

Bedload and suspended load contributions to breaker bar morphodynamics

J. van der Zanden¹, D.A. van der A², D. Hurther³, I. Cáceres⁴, T. O'Donoghue², S.J.M.H. Hulscher¹ and J.S. Ribberink¹.

¹Department of Water Engineering and Management, University of Twente, Netherlands

²School of Engineering, University of Aberdeen, United Kingdom

³Laboratoire des Ecoulements Géophysiques et Industriels LEGI-CNRS, University of Grenoble, France

⁴Laboratori d'Enginyeria Marítima, Universitat Politècnica de Catalunya, Spain

Corresponding author: Joep van der Zanden (j.vanderzanden@utwente.nl)

Highlights:

- ⇒ Laboratory study of sheet flow, suspended and bedload transport, bar evolution, and grain sorting under a plunging wave.
- ⇒ Sheet flow layer dynamics near the breaker bar crest are affected by wave asymmetry but not by wave breaking turbulence.
- ⇒ Onshore bedload and offshore suspended load transport are of similar magnitude across the breaker bar.
- ⇒ Bedload and suspended load transport have opposite effects on breaker bar growth and migration.
- ⇒ Horizontal grain sorting is explained in terms of bedload and suspended load transport.

Keywords:

Breaking wave, sheet flow, breaker bar, morphodynamics, grain size sorting, bedload transport.

Abstract

This study presents measurements of sheet flow processes, grain sorting, and bedload plus suspended load transport rates around a medium-sand breaker bar in a large-scale wave flume. The results offer insights in effects of wave breaking on bedload and grain sorting processes and in the quantitative contributions by bedload and suspended transport to breaker bar morphodynamics. Sheet flow layer dynamics are highly similar to observations under non-breaking waves, revealing clear effects by velocity asymmetry but no evident effects by breaking-generated turbulence, bed slope, or the cross-shore non-uniform flow. The sheet flow layer thickness can be predicted using existing empirical formulations based on local hydrodynamic forcing. At locations covering the shoaling region up to the bar crest the cross-shore variation in bedload transport rates is explained by variations in wave shape (i.e. velocity skewness and asymmetry). At locations between bar crest and bar trough, bedload transport rate magnitudes correlate positively with bed slope and turbulent kinetic energy. Bedload and suspended load transport rates are of similar magnitude but of opposite sign. Bedload transport is onshore-directed and dominates in the shoaling zone, but after wave breaking, the offshore-directed suspended sediment transport increases in magnitude and exceeds bedload transport rates in the breaking and inner surf zones. Bedload and suspended load transport contribute notably differently to bed profile evolution: bedload transfers sand grains from the offshore slope to the bar crest and additionally leads to erosion of the shoreward bar slope and deposition at the bar trough, while suspended load transport induces an opposite pattern of erosion at the bar trough and accretion at the bar crest. Grain size analysis of suspended sediment samples reveals size-selective entrainment and vertical size segregation in the inner surf zone, but suggest size-indifferent entrainment and vertical mixing by energetic vortices in the breaking region. Size-selective transport by bedload and suspended load leads to a cross-shore coarsening of the bed from shoaling to inner surf zone, with local additional sorting mechanisms around the breaker bar due to bed slope effects.

1 **1. Introduction**

2 Breaker bars are morphologic features that are formed naturally in wave breaking zones of dissipative and
3 intermediate beaches (Wright and Short, 1984). Breaker bars enhance wave energy dissipation due to
4 breaking and are one of the factors that determine the state of the beach profile (Lippmann and Holman,
5 1990; Wijnberg and Kroon, 2002; Price and Ruessink, 2011). Bar formation has been explained by the
6 accumulation of shoreward sand transport under shoaling waves and offshore suspended transport under
7 broken waves (Dyhr-Nielsen and Sorensen, 1970; Dally and Dean, 1984). Wave breaking-induced turbulent
8 vortices may locally enhance sand suspension and offshore sand transport rates, resulting in another
9 mechanism for bar formation (Zhang and Sunamura, 1994).

10 Breaker bars are dynamic and tend to migrate offshore during storm conditions, when strong wave breaking
11 occurs, and onshore during mild wave conditions (Thornton *et al.*, 1996; Ruessink *et al.*, 2007). The
12 offshore migration is attributed to an increase in both undertow velocities and suspended sediment
13 concentrations as the intensity of wave breaking increases, which enhances offshore-directed suspended
14 sediment transport (Sallenger *et al.*, 1985; Thornton *et al.*, 1996). Onshore migration is explained by the
15 vertically and horizontally asymmetric ‘sawtooth’ shape of the shoaled waves, leading to higher magnitudes
16 of near-bed orbital velocities (velocity skewness) and of fluid accelerations (acceleration skewness) during
17 the crest phase relative to the trough phase, which both favor onshore-directed wave-related sediment
18 transport near the bed (Elgar *et al.*, 2001; Hoefel and Elgar, 2003). Positive acceleration skewness favors
19 onshore bedload transport as sheet flow through two processes: (i) during the relatively short-duration crest
20 phase, the boundary layer has less time to grow, leading to a velocity gradient $du/d\zeta$ and a bed shear stress
21 (i.e. drag force on particles) with higher crest-phase magnitudes compared to the trough phase (Nielsen,
22 1992; van der A *et al.*, 2011); (ii) pressure forces, that are higher under the steep wave front than at the rear
23 of the wave, contribute to the initial mobilization of bed grains around flow reversal (Drake and Calantoni,
24 2001; Calantoni and Puleo, 2006).

25 By including contributions of offshore-directed current-related and onshore-directed wave-related sediment
26 transport, numerical models can predict on- and offshore bar migration reasonably well (Henderson *et al.*,
27 2004; Hsu *et al.*, 2006; Dubarbier *et al.*, 2015; Fernández-Mora *et al.*, 2015). However, sediment transport
28 predictions in these models are usually only validated on bed profile evolution and may not adequately
29 represent the individual contributions by net bedload and suspended load transport. In addition, the effects
30 of wave breaking on sediment transport rates are not fully understood and therefore often neglected. In
31 order to improve understanding and numerical modeling of breaker bar evolution, it is relevant to study
32 how wave breaking affects bedload transport processes at intra-wave and wave-averaged time scales.

33 Previous research has shown that large-scale wave breaking enhances turbulence levels over the entire
34 water column including the wave bottom boundary layer (van der Zanden *et al.*, 2016). This explains
35 observations of enhanced instantaneous bed shear stresses (Cox and Kobayashi, 2000; Sumer *et al.*, 2013)
36 and suspended sediment entrainment rates (Nielsen, 1984) under breaking waves. The presence of
37 additional turbulence may also increase bedload transport rates, as shown by Sumer *et al.* (2003) for steady
38 flow with artificial grid turbulence. It should be noted that the latter experiment involved mild flow
39 conditions with a bedload transport regime that differs significantly from sheet flow conditions under full-
40 scale breaking waves (Nielsen, 1992). Bedload in sheet flow conditions has been extensively studied in
41 wave flumes under non-breaking waves (Dohmen-Janssen and Hanes, 2002; Schretlen, 2012) and
42 oscillatory flow tunnels (see van der Werf *et al.*, 2009, for an overview). Observations in the swash zone
43 revealed that bore turbulence and cross-shore sediment advection may lead to increased sheet flow layer
44 thicknesses compared to non-breaking wave observations (van der Zanden *et al.*, 2015a; Lanckriet and
45 Puleo, 2015). Due to a lack of high-resolution measurements, it is still unclear if and how wave breaking

46 affects sheet flow transport rates and processes around the breaker bar. Consequently, it is also unclear
47 whether existing engineering-type bedload transport formulae, used for morphodynamic simulations,
48 should account for wave breaking effects (van Rijn *et al.*, 2013). Therefore, the first motivation of the
49 present study is to explore bedload processes across the wave breaking zone.

50 Research has further revealed that transport in the breaking region is size-selective, i.e. differs for each
51 grain size class within a sediment sample. Observations of graded sediment transport under oscillatory sheet
52 flow conditions have shown that coarser grains are transported more easily than finer particles because they
53 are more exposed (de Meijer *et al.*, 2002; Hassan and Ribberink, 2005). The suspended load transport
54 generally contains a relatively high fraction of fine-grained particles which are more easily entrained and
55 mixed than coarse grains (Nielsen, 1992; Wiberg *et al.*, 1994; Davies and Thorne, 2016) and which are
56 advected by the mean current (Sisternans, 2002). In time, the removal of fine-grained particles from the
57 bed may lead to coarsening of the seabed. This may even lead to the formation of erosion-resistant bed
58 surface layers of coarse grains ('armouring'), which can significantly reduce sediment pick-up and transport
59 rates (Nielsen, 1992; Wiberg *et al.*, 1994). Finn *et al.* (2016) suggest, based on detailed simulations with a
60 particle-based numerical model, that for sheet flow conditions such armour layers may already develop
61 after one wave cycle.

62 Grain size observations in the field have revealed a shoreward coarsening of the sand bed due to size-
63 selective transport mechanisms (Murray, 1967; Richmond and Sallenger, 1984). Observations in the field
64 (Wang *et al.*, 1998) and laboratory (Koomans, 2000; Srisuwan *et al.*, 2015; Broekema *et al.*, 2016) have
65 further revealed a relatively large fraction of coarse grains on breaker bar crests, while bar troughs are
66 composed of relatively fine sediment. The transport of graded particles can be modelled by calculating
67 transport for different grain classes independently (e.g. Reniers *et al.*, 2013), with the optional inclusion of
68 a 'hiding/exposure' factor that accounts for reduced or enhanced exposure of certain grain classes (e.g. van
69 Rijn, 2007). The inclusion of size-selective transport can significantly alter numerical predictions of breaker
70 bar position and shape compared to simulations with uniform sand (Van Rijn, 1998; Srisuwan and Work,
71 2015). This illustrates the relevance of grain sorting processes for the understanding and modeling of
72 breaker bar morphodynamics; yet no study has examined the temporal evolution of a breaker bar's grain
73 composition in relation to measured suspended and bedload transport rates. This forms the second
74 motivation of the present study.

75 This study presents high-resolution measurements of sand transport processes under a large-scale laboratory
76 plunging wave and along a fully mobile medium-sand breaker bar. Data from the same experiment were
77 used before to study wave breaking effects on wave bottom boundary layer hydrodynamics (van der Zanden
78 *et al.*, 2016) and on suspension processes (van der Zanden *et al.*, 2017). The present study particularly
79 addresses four matters: (i) the potential effects of wave breaking on sheet flow dynamics, which are
80 measured using a novel conductivity-based concentration measurement system (CCM⁺); (ii) the cross-shore
81 variation in bedload transport rates in relation to the hydrodynamic forcing and to the suspended transport;
82 (iii) the contributions of net bedload and suspended sand transport to the morphological evolution of the
83 breaker bar; (iv) grain size sorting of suspended sediment and of the sand bed.

84 The paper is organized as follows. Section 2 explains the instrument set-up and data treatment steps. Section
85 3 presents the measured bed evolution and the main flow parameters in the experiment. Sheet flow
86 observations and estimated bedload transport rates are presented in Section 4. Section 5 presents and
87 discusses the cross-shore-varying contributions of suspended and bedload transport to breaker bar
88 morphodynamics. Section 6 presents measurements of grain sorting in suspended sediment profiles and
89 along the cross-shore bed profile. Results are discussed in Section 7; Section 8 presents the main
90 conclusions.

91

92 **2. Experimental description**

93 **2.1 Facility and test conditions**

94 The experiments were conducted in the large-scale CIEM wave flume at the Universitat Politècnica de
 95 Catalunya (UPC) in Barcelona. The flume is 100 m long, 3 m wide and 4.5 m deep, and is equipped with a
 96 wedge-type wave paddle. **Figure 1** shows the experimental set-up and bed profile for the present study.
 97 Cross-shore coordinate x is defined positively towards the beach, with $x = 0$ at the toe of the wave paddle.
 98 Vertical coordinate z is defined positively upwards with $z = 0$ at the still water level (SWL). ζ is used for
 99 vertical coordinate positive upwards from the local bed level.

100 The bed profile consisted of medium-grained sand of which the sediment characteristics are detailed in
 101 Section 2.4. The reference bed profile consisted of a bar-trough configuration (**Figure 1a**, black line) that
 102 is roughly divided into an offshore slope of the breaker bar ($x = 35.0$ to 54.8 m; steepness $\tan(\alpha) = 0.10$),
 103 followed by a steeper shoreward-facing bar slope ($x = 54.8$ to 57.5 m; $-\tan(\alpha) = 0.21$), and a mildly sloping
 104 bed shoreward from the bar trough ($x = 57.5$ to 68.0 m; $\tan(\alpha) = 0.01$). The profile shoreward of the mobile
 105 test section ($x > 68.0$ m) followed a slope $\tan(\alpha) = 0.13$, was fixed with geotextile, and was covered with
 106 permeable concrete slabs to promote wave energy dissipation. In this bed configuration, the breaker bar and
 107 trough were deliberately separated from the fixed beach to ensure that the inner surf and swash zone
 108 processes over the sloping beach did not affect the hydrodynamic and sand transport processes in the bar-
 109 trough region.

110 The experiments involved monochromatic waves with wave period $T = 4.0$ s and wave height $H_0 = 0.85$ m
 111 at water depth $h_0 = 2.55$ m near the wave paddle. Table 1 presents an overview of dimensionless parameters
 112 that characterize the wave and beach conditions (c.f. Dean and Dalrymple, 2001). The wave conditions
 113 correspond to a surf similarity parameter $\zeta_0 = 0.54$ and, matching the classification of Battjes (1974),
 114 resulted in plunging breaking waves. The equilibrium beach state (barred or non-barred) can be predicted
 115 based on a combination of parameters. Several indicators for barred profiles have been suggested, i.e. H_0/L_0
 116 $> 5.5\pi w_s/(gT)$ (Kriebel *et al.*, 1986; Dean and Dalrymple, 2001), $H_0/L_0 < 0.0007\Omega^3$ (Kraus and Larson,
 117 1988), and $Pr > 1.0 \cdot 10^4$ (Dalrymple, 1992). Based on each of these three indicators, the present
 118 morphodynamic experiment is expected to produce a barred bed profile (c.f. Table 1).

119 Table 1. Overview of dimensionless parameters that characterize the wave and beach profile conditions.
 120 H_0 and L_0 are the deep-water wave height and wave length, respectively, $\tan(\alpha)$ is the offshore bar slope,
 121 $w_s = 0.034$ m/s is the sand fall velocity, and g is the gravitational acceleration.

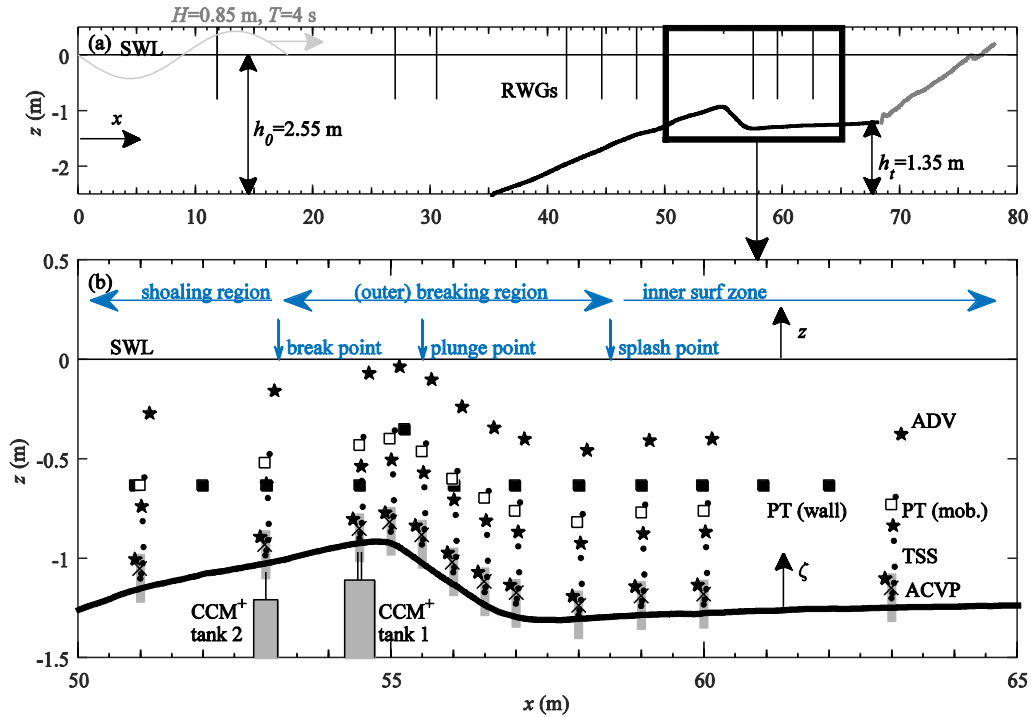
Parameter	Definition	Value
Deep water wave steepness	H_0/L_0	0.034
Surf similarity parameter (Battjes, 1974)	$\zeta_0 = \tan(\alpha)/\sqrt{H_0/L_0}$	0.54
Dean number (Dean, 1973)	$\Omega = H_0/w_s T$	6.3
Fall velocity parameter (Dean, 1973)	$\pi w_s/(gT)$	0.0027
Profile parameter (Dalrymple, 1992)	$Pr = gH_0^2/(Tw_s^3)$	$4.5 \cdot 10^4$
Fall velocity Froude number (Dalrymple, 1992)	$F_w = w_s/\sqrt{gH_0}$	0.20

122

123 Following Svendsen *et al.* (1978), we define the ‘break point’ as the location where the wave starts to
 124 overturn (at $x = 53.0$ m). The ‘plunge point’ ($x = 55.5$ m) is the location where the plunging jet strikes the
 125 water surface (Peregrine, 1983). The ‘splash point’ ($x = 58.5$ m) is the location where the water mass pushed

126 up by the plunging jet strikes the water surface a second time, and where a surf bore starts to develop (Smith
 127 and Kraus, 1991). These regions are used to define the shoaling zone (up to break point; $x \leq 53.0$ m), the
 128 breaking region (between break and splash points; $53.0 < x < 58.5$ m) and the inner surf zone (shoreward
 129 from splash point; $x > 58.5$ m) following Svendsen *et al.* (1978). In **Figure 1b** these points and regions are
 130 included for reference.

131



132

133 Figure 1. Experimental set-up and measurement locations. (a) Reference bed profile (black line) and fixed
 134 beach (grey line), plus locations of resistive wave gauges (RWGs, vertical black lines); (b) Measurement
 135 positions of ADVs (star symbols), mobile-frame Pressure Transducers (PT, white squares), wall-deployed
 136 PTs (black squares), Transverse Suction System nozzles (TSS, black dots), Optical Backscatter Sensor
 137 (black crosses), measuring windows of mobile-frame Acoustic Concentration and Velocity Profiler
 138 (ACVP, grey rectangles) and locations of the two CCM⁺ tanks.

139

140 2.2 Instrumentation

141 Near-bed and outer-flow hydrodynamics and suspended sediment concentrations were measured with a
 142 vertical array of acoustic instruments deployed from a custom-built mobile frame (**Figure 2**). This frame
 143 consisted of stainless-steel tubing with 30 mm diameter and was designed such that it would have minimum
 144 flow perturbation while being sufficiently stiff to withstand wave impact. The frame was mounted to a
 145 horizontally-mobile trolley on top of the flume, and could be vertically positioned with sub-mm accuracy
 146 using a spindle. The mobile frame set-up enabled measurements at various cross-shore positions, while
 147 maintaining an approximately equal elevation of the instrument array with respect to the bed at the start of
 148 each run.

149 The velocity was measured at outer-flow elevations using three acoustic Doppler velocimeters (ADV) and
 150 near the bed with an acoustic concentration and velocity profiler (ACVP), all deployed from the mobile

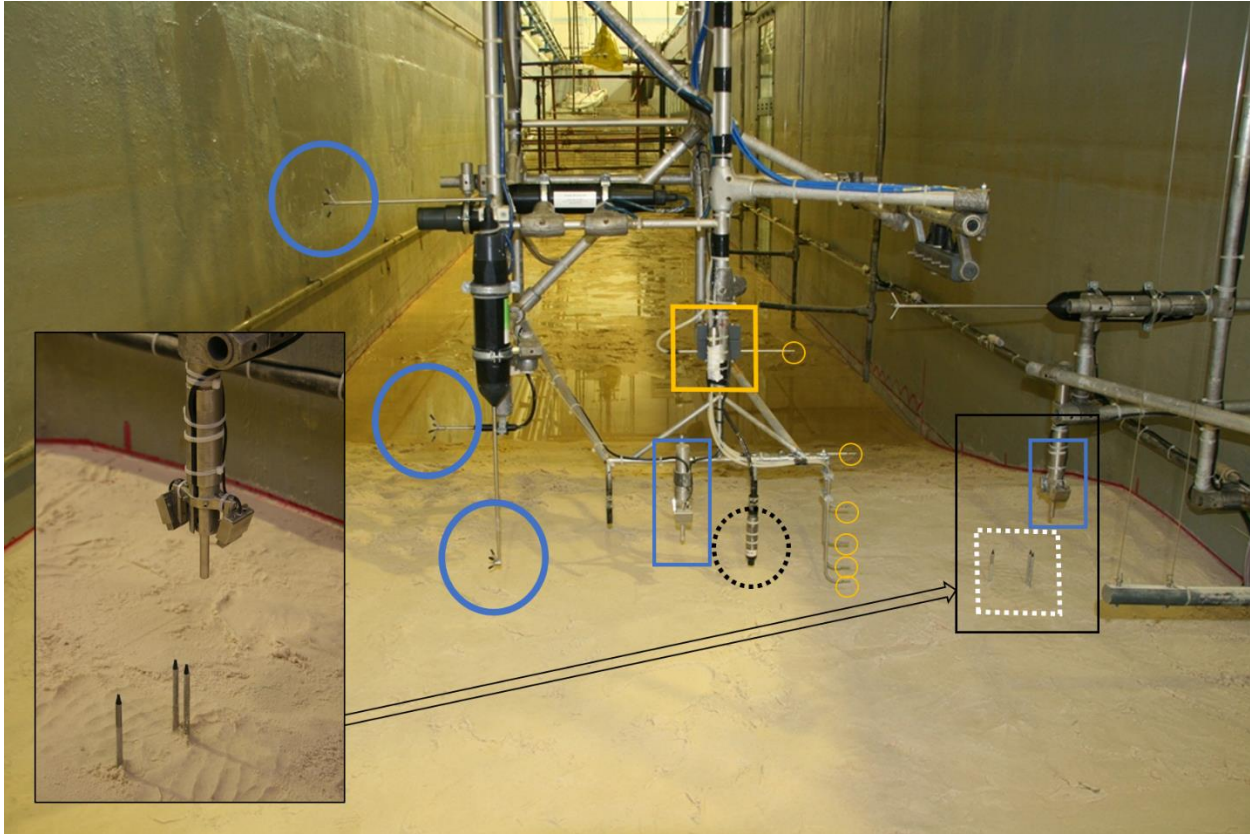
151 frame. The ACVP is a pulse-coherent acoustic Doppler system for measuring co-located particle velocity
152 and sand concentration (Hurther *et al.*, 2011). In the present experiment, the ACVP operated at an acoustic
153 frequency of 1 MHz and measured the two-component (u , w) particle velocity and sand concentration over
154 a 10 to 15 cm vertical profile directly above the bed with 1.5 cm vertical bin resolution and 70 Hz sampling
155 frequency. Sand concentrations were obtained by inverting the reflected ACVP-measured acoustic intensity
156 signal using calibration measurements by a six-nozzle Transverse Suction System (TSS) and an optical
157 backscatter sensor (OBS). The ACVP directly measured the instantaneous horizontal sand flux $\phi_x = uC$,
158 which for the present experiment could be obtained at a measurement frequency of 5 Hz after removal of
159 acoustic Doppler noise contaminations. More details on the velocity, suspended sand concentration, and
160 suspended sand flux measurements can be found in van der Zanden *et al.* (2016; 2017).

161 Time-varying sediment concentrations in the sheet flow layer were measured using two Conductivity-based
162 Concentration Measurement (CCM⁺) tanks (**Figure 1b**). These tanks were located at the bar crest at $x =$
163 53.0 m (at break point where wave starts to overturn) and at $x = 54.5$ m (between break point and plunge
164 point). For the high sand concentrations (100 – 1600 kg/m³) in the sheet flow layer, the measured
165 conductivity of a water-sand mixture is a linear function of sand concentration, which makes the
166 conductivity-based measuring principle highly suitable for studying sheet flow dynamics (Ribberink and
167 Al-Salem, 1995; Dohmen-Janssen and Hanes, 2002; Lanckriet *et al.*, 2013). The CCM⁺ tanks in the present
168 study are equipped with one single conductivity probe plus a combined double probe (for tank 1), or with
169 one single probe (tank 2), and sample with a 1000 Hz data rate. The two sensors of the combined probe of
170 tank 1 (**Figure 2** inset) are spaced 1.5 cm in cross-shore direction and can be used to estimate particle
171 velocities in the sheet flow layer by cross-correlating both sensors' signals (see McLean *et al.*, 2001). The
172 probes penetrate the sheet flow layer from below to minimize flow disturbance.

173 The tanks are equipped with a bed level tracking system that enables automatic repositioning of the probes
174 with sub-mm accuracy and which is fully described in van der Zanden *et al.* (2015a). In tracking mode, the
175 probes track the continuous elevation of the bed-water interface, hence they measure the bed evolution at
176 wave-averaged or longer time scales. Alternatively, the user can select to use the probes to measure sheet
177 flow concentrations at a fixed absolute elevation (i.e. no tracking). In the present study, both types of
178 measurements were alternated for fixed intervals of 60 s: sheet flow concentration measurements were
179 obtained at elevations of -2, +0, and +4 mm with respect to the bed; after each of these intervals, the probes
180 were repositioned to the local bed level by activating the tracking system. Through this procedure,
181 concentrations were sampled over the complete sheet flow layer while at the same time the bed level was
182 measured with +/- 1 mm accuracy.

183 A six-nozzle Transverse Suction System (TSS) was used to collect samples of suspended sediment at $\zeta \approx$
184 0.02, 0.04, 0.10, 0.18, 0.31 and 0.53 m (see van der Zanden *et al.*, 2017, for more details). The collected
185 samples were dry-weighed and packed. The grain size characteristics were determined at the University of
186 Aberdeen using a Beckman Coulter LS 13 320 laser diffraction particle sizer (specifications found in the
187 user manual: Beckman Coulter Inc, 2008). Previous experience using this particle sizer indicated a
188 minimum amount of 2.5 g sand (corresponding to obscuration > 5%) to be required for a reliable estimate
189 of the size distribution. This minimum amount was reached for all TSS samples, except for some of the
190 samples obtained at the furthest offshore location ($x = 51.0$ m) or at elevations above wave trough level.
191 For these combinations of locations/nozzles, samples of different runs but for the same nozzle and cross-
192 shore location were combined to obtain the required amount of sand.

193



194

195 Figure 2. Mobile measuring frame and instrumentation. Instrumentation includes three acoustic Doppler velocimeters (ADV,
 196 blue solid circles), one pressure transducer (PT, yellow square), a six-nozzle transverse suction system (TSS, yellow circles), an
 197 optical backscatter sensor (dashed circle) and an acoustic concentration and velocity profiler (ACVP, blue rectangle). Inset shows
 198 close-up of CCM⁺ tank 1 sensors (dashed square) and another ACVP, deployed from the sidewall. Note that the CCM⁺ sensors
 199 are raised here above the bed; during the experiment the tops of the sensors are within +/- 1 cm from the bed.

200

201 Water surface elevation was measured with a combination of resistive wave gauges (RWGs) in the shoaling
 202 zone and pressure transducers (PTs) in the breaking and inner surf zone. Bed profile measurements were
 203 obtained at 2 cm cross-shore resolution along two transects, at lateral distances of 0.1 and 0.7 m at either
 204 side of the flume's centerline, using echo sounders deployed from a second mobile trolley. The echo
 205 sounders had an estimated accuracy of +/- 1 cm and the mean of both sensors is used to study the bed
 206 profile evolution and net sediment transport rates.

207

208 2.3 Measurement procedure

209 One experiment consisted of 90 minutes of waves, divided over six 15-minute runs, during which the bed
 210 profile evolved. The bed profile was measured prior to the first run and after every 2nd run, i.e. at $t = 0, 30,$
 211 60 and 90 minutes. After the sixth run, the flume was drained. The reference bed profile, drawn as template
 212 on the flume wall, was then restored by shoveling back the transported sand and flattening any bed forms
 213 that were generated. Each experiment was repeated 12 times, with the mobile measuring frame positioned
 214 at a new location for each experiment. The bed profile evolution and hydrodynamics were very similar for
 215 each experiment (van der Zanden *et al.*, 2016) and the adopted procedure resulted in a high spatial coverage
 216 of velocity and concentration measurements (**Figure 1b**).

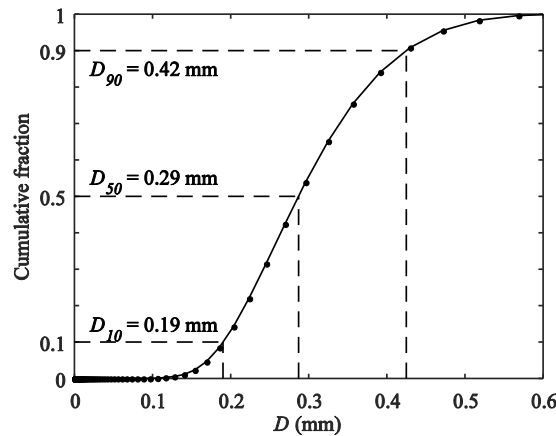
217 Sediment samples of the bed were taken at 12 cross-shore locations at the start of the campaign
 218 (corresponding to horizontal test section), after the initial start-up stage (corresponding to reference bed
 219 level and $t = 0$ min.) and at the end of the final experimental repeat ($t = 90$ min.). Bed samples were taken
 220 at each cross-shore location by carefully scraping off the upper 1 to 2 cm of the sand bed at three positions
 221 separated in cross-flume direction. In the inner surf zone, where bed forms occurred, the samples were
 222 taken over a complete ripple length. When restoring the profile, the sediment was reshuffled by bringing
 223 sediment from the shoaling to the inner surf zone and vice versa.

224

225 **2.4 Sediment characteristics**

226 **Figure 3** shows the cumulative grain-size distribution measured with the laser-diffraction particle sizer for
 227 one of the bed samples at the start of the campaign. The accordingly obtained median sediment diameter
 228 (D_{50}) is 0.29 mm. This is somewhat higher than values of 0.25 mm found for the exact same sediment by
 229 independent sieving tests at the CIEM lab and by sieving tests by the sediment supplier. This difference is
 230 explained by sand grains not being perfect spheres: the particle sizer measures an equivalent ‘perfect sphere’
 231 diameter; sieving yields the diameter of the smallest cross-sectional area of a non-spherical grain (Eshel *et*
 232 *al.*, 2004). The degree of uniformity is quantified through the geometric method of moments σ_g (Blott and
 233 Pye, 2001). With a measured $\sigma_g = 1.36$, the sand is classified ‘well sorted’ following Blott and Pye (2001).
 234 The sand grains had a measured mean settling velocity $w_s = 0.034$ m/s.

235



236

237 Figure 3: Cumulative grain-size distribution of bed sediment at the start of the experiment (obtained by
 238 the laser-diffraction particle sizer).

239

240 **2.5 Data treatment**

241 Data treatment steps related to hydrodynamics and suspended sediment concentrations and fluxes is
 242 described extensively in van der Zanden *et al.* (2016; 2017). These steps are only briefly repeated here.

243 Visual observations and measurements revealed that a hydrodynamic equilibrium established for each run
 244 after approximately 5 minutes. Therefore, only the last 10 minutes of data from each run (corresponding to
 245 about 150 wave cycles) were used for analysis. Flume seiching induced a standing wave with an
 246 approximately 45-s period. The seiching wave could be identified in auto-spectra of water surface and
 247 horizontal velocities, but not in bed level and suspended sediment concentrations. Hence, its effect on

248 sediment processes is considered negligible. The standing wave was removed from water surface and
 249 velocity time series by applying a high-pass filter with a cut-off frequency of 0.125 Hz (half the primary-
 250 wave frequency).

251 The phase-averaged value of a variable ψ are annotated with angle brackets and are calculated over N wave
 252 repetitions as

$$253 \quad \langle \psi \rangle(t) = \frac{1}{N} \sum_{n=1}^N \psi(t+(n-1)T) \quad (1).$$

254 Reference zero-up crossings, required to phase-reference each wave cycle prior to phase-averaging, were
 255 based on water surface measurements at $x = 47.6$ m. Data were phase-referenced such that $t/T=0$
 256 corresponds to maximum surface elevation (wave crest) at the beginning of the test section ($x = 50.0$ m).
 257 Phase-averaged horizontal velocities $\langle u \rangle$ consist of a time-averaged component \bar{u} , i.e.

$$258 \quad \bar{u} = \frac{1}{T} \int_0^T \langle u(t) \rangle dt \quad (2),$$

259 and a periodic component $\tilde{u} = \langle u \rangle - \bar{u}$. Root-mean-squared \tilde{u} is denoted \tilde{u}_{rms} . The turbulent velocity
 260 components u' , v' , w' were obtained through a Reynolds decomposition based on the phase-average, i.e. u'
 261 $= u - \langle u \rangle$, and were subsequently used to calculate the phase- and time-averaged turbulent kinetic energy
 262 (TKE). Note that following this definition for u' , the phase-coherent motion of the plunging jet is part of
 263 the period component \tilde{u} and does not contribute to TKE. More details on turbulence data processing are
 264 given by Van der Zanden *et al.* (2016).

265 The CCM⁺ tanks were positioned at fixed cross-shore locations during the experiment. Measurements were
 266 phase-averaged for each 15-min. stage of bar development over all 12 experimental repeats, resulting in a
 267 large number of wave repetitions ($N > 1000$). For the time-varying sheet flow concentration measurements
 268 $C(\zeta, t)$, $\zeta=0$ is defined as the bed level during the zero-down crossing of the wave when the bed is considered
 269 to be at rest ('immobile bed level'). Intra-wave bed level fluctuations are preserved in phase-averaged
 270 results. $C(\zeta, t)$ measurements were bin-averaged, where the bin class was based on the relative elevation ζ
 271 and the bin resolution $\Delta\zeta = 0.25$ mm. For each wave phase and elevation bin, $\langle C(\zeta_i, t) \rangle$ is calculated as the
 272 median of concentration measurements in the range $\zeta_i - \Delta\zeta/2 < \zeta_i < \zeta_i + \Delta\zeta/2$.

273 For calculating sand particle velocities in the sheet flow layer, the concentration time series of the two
 274 sensors of the combined probe were first high-pass filtered ($f_{cutoff} = 1$ Hz). The cross-correlation of the two
 275 sensors' signals was calculated over regular time intervals $\Delta t = 0.1$ s. Each wave cycle was assigned a
 276 concentration bin class (bin resolution $\Delta C = 0.1$ m³/m³) based on wave-averaged concentration. The cross-
 277 correlation output was then averaged for each ΔC bin class and each wave phase $\Delta t/T$. The bin-averaged
 278 cross-correlation is used to quantify the time lag between both signals, which with known distance between
 279 the sensors is translated into a particle velocity (see further McLean *et al.*, 2001; van der Zanden *et al.*,
 280 2015a).

281 Volumetric total sediment transport rates q_{tot} , due to contributions by both bedload and suspended load, can
 282 be obtained from measured bed profile measurements z_{bed} by solving the Exner equation:

$$283 \quad q_{tot}(x) = q_{tot}(x - \Delta x) + \Delta x(1 - \varepsilon_0) \frac{\Delta z_{bed}(x)}{\Delta t} \quad (3).$$

284 Here, ε_0 is the sand porosity (0.4 if loosely packed), Δx is the horizontal resolution of z_{bed} measurements
 285 ($=0.02$ m) and Δt is the time interval between two consecutive profile measurements (30 min.). Equation 3
 286 can be solved if q_{tot} is known at one x location. With $q_{\text{tot}} = 0$ at the left-hand (i.e. $x = 35$ m) and right-hand
 287 boundary ($x = 68$ m) of the mobile test section, q_{tot} can be solved iteratively by starting from either the left-
 288 or the right-hand side of the profile. This yields two estimates of q_{tot} , annotated q_{lhs} and q_{rhs} respectively.
 289 The estimates q_{lhs} and q_{rhs} are likely different due to variations in the horizontally-integrated volume of the
 290 two profile measurements used to quantify Δz_{bed} . These variations can be attributed to sampling errors of
 291 the acoustic sensors, 3D bed forms, variations in packing density and porosity, and non-uniformity of the
 292 bed profile (e.g. Baldock *et al.*, 2011). For the present experiment, the cross-shore-integrated measured bed
 293 profile increased on average by 0.22 m^2 between the start and end of the experiment, which is equivalent
 294 to a mean overestimation of $\Delta z_{\text{bed}}(x)$ by 0.007 m at the end of the experiment. This increase can be attributed
 295 to scouring that occurred near the flume side-walls and which resulted in sand accumulation around the
 296 centerline of the wave flume, where the profile was measured.

297 Although the systematic error of 0.007 m in Δz_{bed} is considered small compared to the main bed level
 298 changes during the experiment (Δz_{bed} of $O(0.1 \text{ m})$), it leads to a significant cumulative error in $q_{\text{tot}}(x)$ (up to
 299 $2 \cdot 10^{-5} \text{ m}^2/\text{s}$). Depending on distance to each horizontal boundary of the test section, q_{lhs} or q_{rhs} is more
 300 accurate. The error in the volumetric total transport rate q_{tot} can therefore be minimized by calculating the
 301 weighted average of both estimates:

$$302 \quad q_{\text{tot}}(x) = \left(\frac{x_{\text{end}} - x}{x_{\text{end}} - x_0} \right) q_{\text{lhs}}(x) + \left(\frac{x - x_0}{x_{\text{end}} - x_0} \right) q_{\text{rhs}}(x) \quad (4),$$

303 with $x_0 = 35$ m and $x_{\text{end}} = 68$ m being the left- and right-hand boundary of the mobile bed profile,
 304 respectively. The transport rate $q_{\text{tot}}(x)$ was calculated for each experimental repeat using Eq. (3) and (4),
 305 and was then averaged over all repeats. The resulting estimated error in q_{tot} varies between 0 and $1 \cdot 10^{-5}$
 306 m^2/s , with smallest values at the left- and right-hand boundaries and highest values for the middle of the
 307 test section.

308

309 **3. Hydrodynamics and bed profile evolution**

310 This section presents an overview of the main hydrodynamics and the bed profile evolution. The reader is
 311 referred to van der Zanden *et al.* (2016) for a more detailed description of the near-bed hydrodynamics
 312 (including turbulence) in the present experiment and to van der A *et al.* (2017) for an extensive analysis of
 313 the outer-flow hydrodynamics for an accompanying rigid-bed experiment with the same bed profile and
 314 wave conditions.

315

316 **3.1 Hydrodynamics**

317 **Table 2** presents an overview of the main hydrodynamic parameters at the 12 measurement locations.
 318 **Figure 4a** shows the wave crest and trough levels and the time-averaged water level $\bar{\eta}$. The wave height (H
 319 $= \eta_{\text{crest}} - \eta_{\text{trough}}$) reduces by 50% between the break point (around $x = 53.0$ m) and splash point ($x = 58.5$ m).
 320 Water levels $\bar{\eta}$ show a set-down at the shoaling locations and set-up at the inner surf zone. **Figure 4b** shows
 321 time-averaged velocity \bar{u} and maximum onshore and offshore horizontal velocity $\langle u \rangle_{\text{max}}$ and $\langle u \rangle_{\text{min}}$. These
 322 values are measured at the wave bottom boundary layer (WBL) overshoot elevation δ ($\zeta \approx 0.02$ m) and are
 323 averaged over the complete experiment ($t = 0 - 90$ min., i.e. over six runs). Along the offshore slope up to
 324 the bar crest ($x=51.0 - 55.0$ m), $\langle u \rangle_{\text{max}}$ and $\langle u \rangle_{\text{min}}$ remain roughly constant. Time-averaged velocity
 325 magnitudes are lowest at $x = 51.0$ m and increase towards the bar crest. The skewness and asymmetry of \bar{u}

326 (Table 2) show that the intra-wave shape of \tilde{u} changes significantly along the offshore slope. Most notable
 327 is the large asymmetry at $x = 53.0$ m at the onset of breaking-wave overturning. Along the shoreward-facing
 328 bar slope ($x = 55.5$ to 58.0 m), the combination of decreasing H and increasing h leads to a substantial
 329 decrease in orbital velocity amplitude while at the same time the magnitudes of offshore-directed time-
 330 averaged velocity \bar{u} (undertow) increases. Undertow velocity magnitudes decrease again in the inner surf
 331 zone ($x > 58.5$ m).

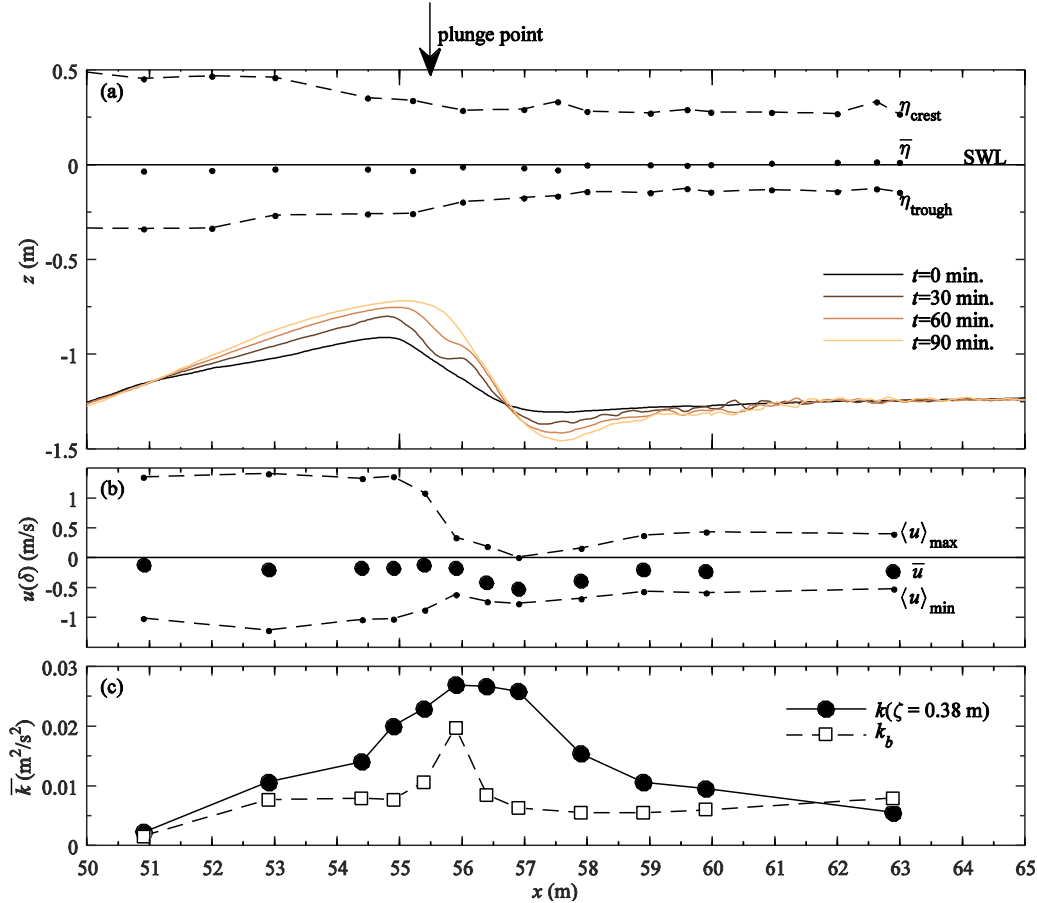
332 Table 2. Hydrodynamic and bed parameters at each measurement location: water depths (h); wave heights
 333 (H); ADV-measured velocity statistics at $\zeta=0.11$ m, with maximum onshore and offshore phase-averaged
 334 horizontal velocity, semi-excursion length ($a = \sqrt{2}T\tilde{u}_{rms}/2\pi$), velocity skewness ($Sk(u) = \bar{\tilde{u}^3}/\tilde{u}_{rms}^3$),
 335 velocity asymmetry ($Asy(u) = -\overline{H\tilde{u}^3}/\tilde{u}_{rms}^3$, where H marks Hilbert transform (e.g. Elgar, 1987), local
 336 bed slope $\tan(\alpha) = dz_{bed}/dx$ at the start ($t = 0$ min.) and end ($t = 90$ min.) of the experiment. The listed
 337 hydrodynamic parameters were measured during the first run of each experimental repeat ($t = 0 - 15$
 338 min.).

x (m)	h (m)	H (m)	\bar{u} (m/s)	$\langle u \rangle_{max}$ (m/s)	$\langle u \rangle_{min}$ (m/s)	a (m)	$Sk(u)$	$Asy(u)$	$\tan(\alpha),$ $t=0$ min.	$\tan(\alpha),$ $t=90$ min.
51.0	1.10	0.79	-0.13	1.04	-0.83	0.54	0.61	0.68	0.08	0.12
53.0	0.97	0.74	-0.22	0.80	-0.94	0.48	0.44	1.01	0.06	0.12
54.5	0.88	0.64	-0.19	0.84	-0.85	0.47	0.50	0.82	0.04	0.06
55.0	0.88	0.60	-0.24	0.78	-0.90	0.47	0.48	0.76	-0.10	0.03
55.5	0.97	0.51	-0.23	0.57	-0.83	0.39	0.36	0.75	-0.22	-0.12
56.0	1.10	0.50	-0.30	0.25	-0.82	0.31	0.06	0.77	-0.20	-0.45
56.5	1.19	0.53	-0.51	0.05	-0.83	0.25	0.67	0.76	-0.18	-0.51
57.0	1.24	0.48	-0.54	0.02	-0.78	0.23	0.95	0.58	-0.08	-0.35
58.0	1.28	0.47	-0.46	0.01	-0.71	0.21	0.82	0.79	0.02	0.11
59.0	1.28	0.43	-0.36	0.13	-0.71	0.23	0.39	0.88	0.02	0.16
60.0	1.26	0.42	-0.36	0.17	-0.66	0.24	0.67	0.68	0.03	0.02
63.0	1.26	0.41	-0.34	0.19	-0.58	0.23	0.79	0.45	0.01	0.01

339
 340 **Figure 4c** shows the time-averaged TKE (\bar{k}) at outer-flow elevation and close to the bed. The latter, k_b , is
 341 defined here as the maximum \bar{k} measured inside the WBL. Turbulence production by wave breaking leads
 342 to large magnitudes of outer-flow \bar{k} near the plunge point at $x = 55.5$ m. \bar{k} decreases towards the bed at most
 343 locations, which indicates that wave breaking is the primary source of turbulence. Breaking-generated
 344 turbulence is advected to offshore locations while gradually dissipating, and consequently, \bar{k} decreases from
 345 the breaking zone in offshore direction (from $x = 55.5$ to 51.0 m). Turbulent kinetic energy inside the WBL
 346 (k_b) follows a similar cross-shore pattern as outer-flow \bar{k} , i.e. it increases by an order of magnitude between
 347 the shoaling zone at $x = 51.0$ m to the breaking region at $x = 56.0$ m. This increase occurs in spite of a
 348 decrease in $\langle u \rangle_{max}$ and $\langle u \rangle_{min}$, which suggests that the increase in k_b is due to the invasion of breaking-
 349 generated turbulence into the WBL. Further shoreward, k_b decreases above the bar trough (around $x = 58.0$
 350 m) and increases gradually throughout the inner surf zone ($x > 58.5$ m) due to the presence of sand ripples.

351 Flow disturbance by the mobile frame contributed locally to the measured TKE. The contributions of frame-
 352 generated turbulence to TKE were assessed by inter-comparing velocity measurements that were collocated

353 at x, z coordinates but positioned at different cross-flume distances from the frame (van der A *et al.*, 2017).
 354 Notable contributions of frame-generated turbulence to ADV-measured TKE appeared only at locations
 355 where other sources of turbulence (bed friction and wave breaking) were small: at $x = 51.0$ m (shoaling
 356 zone) and $x > 60.0$ m (inner surf zone).



357
 358 Figure 4. (a) Bed profile evolution (solid lines, with each line representing the mean value over all
 359 experimental days), and water levels for $t = 0$ –15 min. (dots and dashed lines depict time-averaged and
 360 envelope, respectively); (b) ACVP-measured horizontal velocity at the WBL overshoot elevation $\zeta = \delta$,
 361 for $t = 0$ –90 min., time-averaged (circles) and maximum phase-averaged onshore and offshore velocity
 362 (dots and dashed line); (c) Time-averaged turbulent kinetic energy over the experiment ($t = 0$ –90 min.) at
 363 outer-flow elevation $\zeta = 0.38$ m (measured with ADV, solid line + circles) and inside the WBL (measured
 364 with ACVP, dashed line + squares).

365 3.2 Bed profile evolution and net total transport

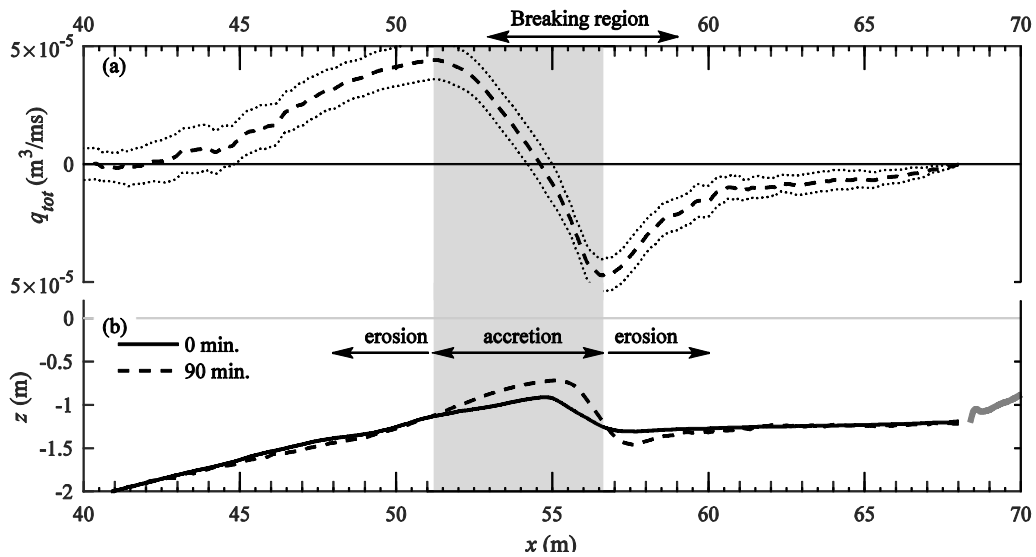
366 **Figure 4a** shows the bed profile evolution. The bar crest grows and migrates slightly onshore during the
 367 experiment. This leads to an increase in the bar's offshore slope from $\tan(\alpha) = 0.10$ to 0.13 and an increase
 368 in the surf similarity parameter ζ_0 from 0.54 to 0.68. At the same time the bar trough deepens, resulting in
 369 a steepening of the shoreward slope of the breaker bar from $\tan(\alpha) = -0.21$ to -0.47 . At $t = 90$ minutes, this
 370 slope approaches the natural angle of repose ($\tan(\alpha) \approx 0.5$ to 0.7) for sandy materials (Nielsen, 1992). **Table**
 371 **2** includes the local bed slope at the start and end of the experiment for each measurement location.

372 Bed forms were observed after draining the flume. The bed was flat in the shoaling region and at the bar
 373 crest ($x = 48.0$ to 55.5 m), indicating bedload transport in the sheet flow regime. Quasi-2D bed forms (quasi-

374 uniform in cross-flume direction) were identified along the shoreward slope of the bar ($x = 55.5$ to 57.0 m),
 375 where they migrated progressively offshore. These bed forms were asymmetrically shaped, with a relatively
 376 steep offshore slope and a mild shoreward slope. Shoreward-facing lunate-shaped bed forms were formed
 377 at the bar trough ($x = 57.0$ to 59.0 m). At the inner surf zone a gradual transition to quasi-2D bed features
 378 occurs (from $x = 59.0$ to 62.0 m). Further shoreward these features became increasingly irregular while
 379 their wave length reduced, resulting in 3D sand ripples ($x = 62.0$ m to 68.0 m). In the inner surf zone ($x >$
 380 58.5 m) bed form lengths were of similar magnitude as the orbital semi-excursion length a . The bed forms
 381 in the breaking region had lengths that exceed a by a factor 2 to 5.

382 The bar growth can be explained by accumulation of primarily onshore-directed total transport at shoaling
 383 locations and offshore-directed transport in the breaking and inner surf zone (**Figure 5**). The reversal of
 384 transport direction occurs near the breaker bar crest ($x = 54.5$ m), about 1 m offshore from the plunge point.
 385 The sharp gradients dq_{tot}/dx at the breaking region indicate strong cross-shore non-uniformity in sand
 386 transport processes. Note that q_{tot} is not constant throughout the experiment; instead, the magnitudes of
 387 onshore and offshore q_{tot} decrease as the breaker bar evolves towards a semi-equilibrium state (Van der
 388 Zanden *et al.*, 2015b). This morphologic feedback of profile evolution on time-evolving transport rates is
 389 not further considered in the present study.

390



391

392 Figure 5. (a) Total transport during the experiment ($t = 0$ – 90 min.) obtained through Eq. (4), mean values
 393 (dashed) $\pm 95\%$ confidence interval (dotted) over all experimental repeats; (b) Initial (solid) and final
 394 (dashed) bed profile. The grey shading marks the region of net accretion.

395

396 4. Bedload transport processes

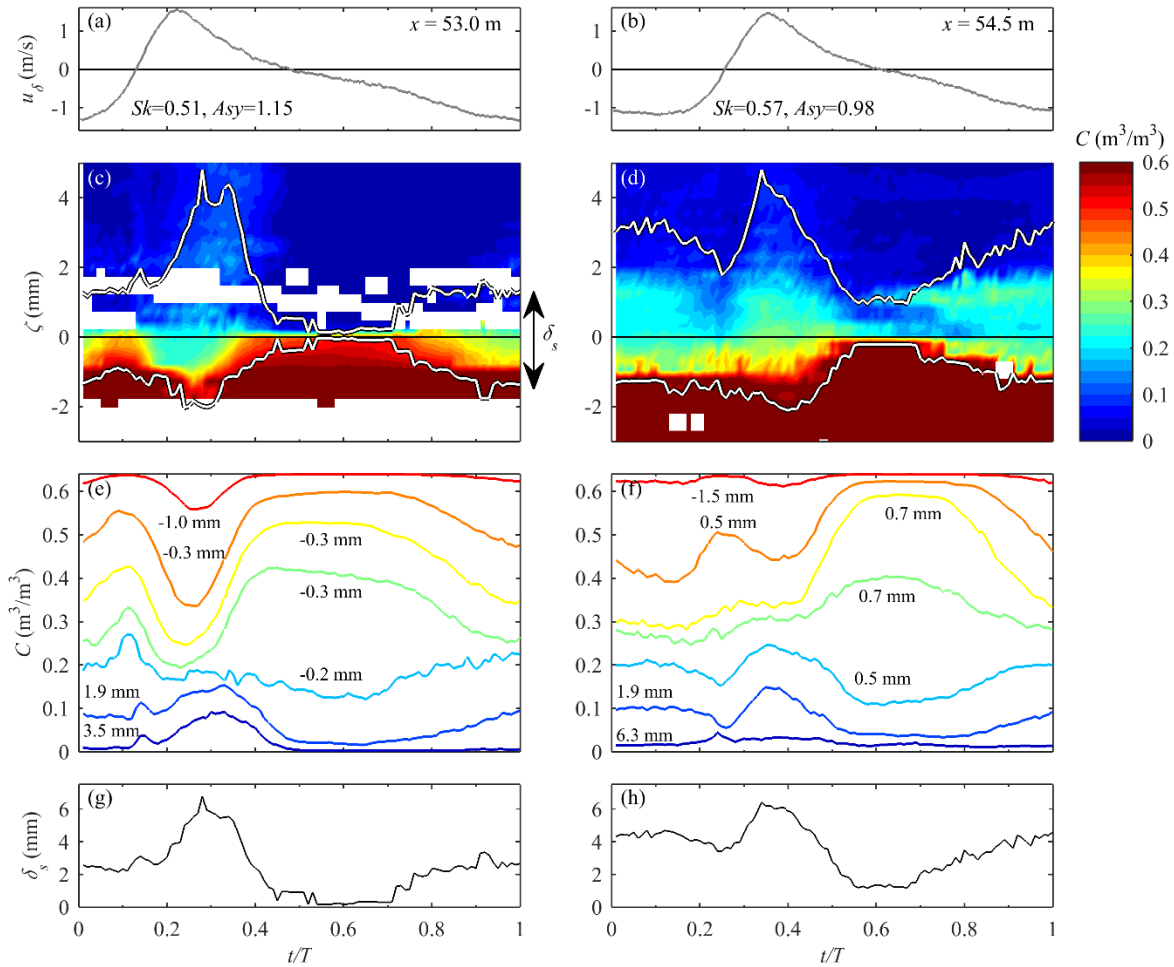
397 This section first presents and discusses sheet flow measurements (Sections 4.1 to 4.3) which are compared
 398 with oscillatory sheet flow observations in tunnels and under non-breaking waves to assess the effects of
 399 wave breaking. Next, Section 4.4 presents the cross-shore-varying bedload transport rates and relates these
 400 to the near-bed hydrodynamics.

401

402 **4.1 Sheet flow layer concentrations**

403 The sheet flow layer behavior is explored using CCM⁺ measurements at two locations near the breaker bar
404 crest, i.e. at $x = 53.0$ m (below break point) and $x = 54.5$ m (between break point and plunge point). **Figure**
405 **6c,d** shows phase-averaged concentrations $\langle C(\zeta, t) \rangle$, bin-averaged for vertical elevations ζ with bin
406 resolution $\Delta\zeta = 0.25$ mm and based on a minimum of three wave repetitions. Due to the chosen settings for
407 probe repositioning during acquisition, this minimum was not obtained for each ζ bin class (which explains
408 the data gaps e.g. at $\zeta \approx 2$ mm, **Figure 6c**). **Figure 6e,f** also shows concentration time series, but for these
409 panels C was phase-averaged for seven bins based on the wave-averaged concentration for each wave cycle.
410 The latter data representation preserves the temporal variation in C that occurs at intra-wave time scale and
411 it has been adopted throughout many sheet flow studies (Ribberink and Al-Salem, 1994; O'Donoghue and
412 Wright, 2004; Schretlen, 2012). This approach is especially useful to study phase lags between the upper
413 sheet flow layer (region above the 'immobile bed level', i.e. $\zeta > 0$, with typical concentrations lower than
414 $0.3 \text{ m}^3/\text{m}^3$) and the erosion layer ($\zeta < 0$, $C > 0.3 \text{ m}^3/\text{m}^3$).

415 Despite sheet flow layers being rather thin, of $O(\text{mm})$, the CCM⁺ manages to resolve the time-varying
416 concentrations adequately. This is partly ascribed to the new automatic probe repositioning system, which
417 allows measurements of the time-varying relative bed level with higher accuracy than previous versions of
418 the CCM system. At both CCM⁺ locations, instances of peak offshore and onshore velocities lead to a quasi-
419 instantaneous concentration decrease in the erosion layer ($C < 0.3 \text{ m}^3/\text{m}^3$) and a simultaneous increase in
420 the upper sheet flow layer ($C < 0.3 \text{ m}^3/\text{m}^3$). The erosion layer responds layer by layer to velocity forcing,
421 i.e. concentrations at elevations deeper in the erosion layer ($\zeta \approx -2$ to -1 mm) respond slightly later than
422 concentrations near $\zeta = 0$. Hence, no evidence of a rapid pressure-induced mobilization of a complete
423 'block' of sediment ('plug flow', c.f. Sleath, 1999) is found. The short increase in upper sheet flow layer
424 sediment concentration around flow reversal ($t/T = 0.17$) at $x = 53.0$ m has also been observed in oscillatory
425 sheet flow conditions and may relate to shear instabilities around flow reversal (Ribberink and Al-Salem,
426 1995; O'Donoghue and Wright, 2004).



427

428 Figure 6. Time series of phase-averaged CCM⁺ measurements at $x = 53.0$ m (left) and $x = 54.5$ m (right),
 429 for final stage of bar development ($t = 75\text{--}90$ min). (a,b) ACVP-measured velocities at $\zeta = \delta$, including
 430 non-dimensional velocity skewness (Sk) and acceleration skewness (Asy) values. (c,d) Concentration
 431 contour, with white lines marking the erosion depth and the top of the sheet-flow layer; (e,f)
 432 Concentration time series, phase-averaged for 7 wave-averaged concentration bins. For each
 433 concentration bin, the calculated relative position ζ (standard deviation ± 1 mm) is indicated in the
 434 panels; (g,h) Sheet flow layer thickness.

435

436 4.2 Sheet flow layer thickness

437 The time-varying sheet flow layer δ_s is the difference between the intra-wave time-varying bottom (i.e.
 438 erosion depth) and the top of the sheet flow layer (i.e. the elevation with $\langle C \rangle = 0.08$ m^3/m^3 ; Dohmen-
 439 Janssen and Hanes, 2002). These elevations were established by fitting the empirical function of
 440 O'Donoghue and Wright (2004) for vertical sheet flow concentration profiles through the time-varying
 441 concentration measurements (the approach is described more extensively in Van der Zanden *et al.*, 2015a).
 442 The function fitted well through the measurements ($r^2 > 0.9$ for each profile). **Figure 6c,d** includes the time-
 443 varying erosion depth and top of the sheet flow layer and **Figure 6g,h** shows the intra-wave sheet flow
 444 thickness δ_s .

445 The sheet flow thickness shows similar phase behavior as the near-bed velocity magnitude, which again
 446 illustrates the quasi-instantaneous response of sheet flow pick-up to near-bed velocity. At $x = 53.0$ m, δ_s
 447 returns to near zero during the crest-to-trough flow reversal, which indicates that most of the sediment that
 448 was entrained from the bed to the upper sheet flow layer during the crest phase, has settled down once the
 449 flow reverses. At $x = 54.5$ m, δ_s is about 1.5 mm (i.e. non-zero) during the crest-to-trough flow reversal,
 450 possibly due to the significant deposition rate (about -0.2 kg/m²s) of suspended sediment at this location
 451 during this phase of the wave cycle (van der Zanden *et al.*, 2017).

452 At both locations, the non-zero δ_s around trough-to-crest flow reversal indicates that a fraction of sediment
 453 particles that have been entrained during the trough phase has not fully settled as the crest phase begins.
 454 This lagging of sheet flow layer concentration is caused by the relatively short time interval between
 455 maximum offshore and maximum onshore velocities in highly acceleration-skewed flows (Watanabe and
 456 Sato, 2004; Van der A *et al.*, 2009; Ruessink *et al.*, 2011). Maximum sheet flow thicknesses at both
 457 locations are higher during the crest than during the trough phase. Especially at $x = 53.0$ m (breaking point),
 458 where highest wave steepness and near-bed acceleration skewness were measured, a large mobilization of
 459 sand particles which contributes to onshore transport occurs during the wave crest phase. Such asymmetry
 460 in sheet flow thickness has been shown before for positively velocity- and acceleration-skewed flow
 461 conditions in an oscillatory flow tunnel (Ruessink *et al.*, 2011) and can be explained by pressure-force-
 462 induced sand mobilization under the wave front (Drake and Calantoni, 2001; Calantoni and Puleo, 2006)
 463 and to a higher bed shear stress during the crest phase (van der A *et al.*, 2011). Which of these two processes
 464 is dominant in the present experiment, cannot be concluded based purely on these measurements but would
 465 require a detailed numerical assessment of all forces, which besides the fluid-particle forces also includes
 466 the inter-particle interaction forces (c.f. Drake and Calantoni, 2001; Calantoni and Puleo, 2006).

467 To assess whether wave breaking affects the sheet flow layer thickness, δ_s is quantitatively compared with
 468 predictions by two empirical formulations for maximum δ_s that have been proposed on the basis of detailed
 469 laboratory measurements using well-sorted sand and regular oscillatory and wave conditions: firstly, the
 470 formulation by Ribberink *et al.* (2008) based on oscillatory flow tunnel data:

$$471 \quad \delta_s/D_{50} = 10.6 \theta \quad (5),$$

472 and secondly, Schretlen's (2012) formulation based on uniform non-breaking waves measurements:

$$473 \quad \delta_s/D_{50} = 13.1 \theta^{0.7} \quad (6).$$

474 The Shields parameter θ is the non-dimensional bed shear by phase-averaged velocities, i.e. $\theta = \tau_b/(\rho_s -$
 475 $\rho)gD_{50}$, with ρ_s ($=2650$ kg/m³) and ρ ($=1000$ kg/m³) being the densities of sediment particles and water,
 476 respectively, and g ($=9.81$ m/s²) is the gravitational acceleration. The bed shear stress τ_b is estimated based
 477 on the horizontal velocity at $\zeta = \delta$ through $\tau_b = 0.5f_{wc}u(\delta)^2$. The methodology described by Ribberink (1998)
 478 is applied to calculate the wave-plus-current friction factor f_{wc} as a linear combination of the wave friction
 479 factor f_w and the current friction factor f_c . The wave friction factor f_w is calculated based on the widely used
 480 formulation by Swart (1974):

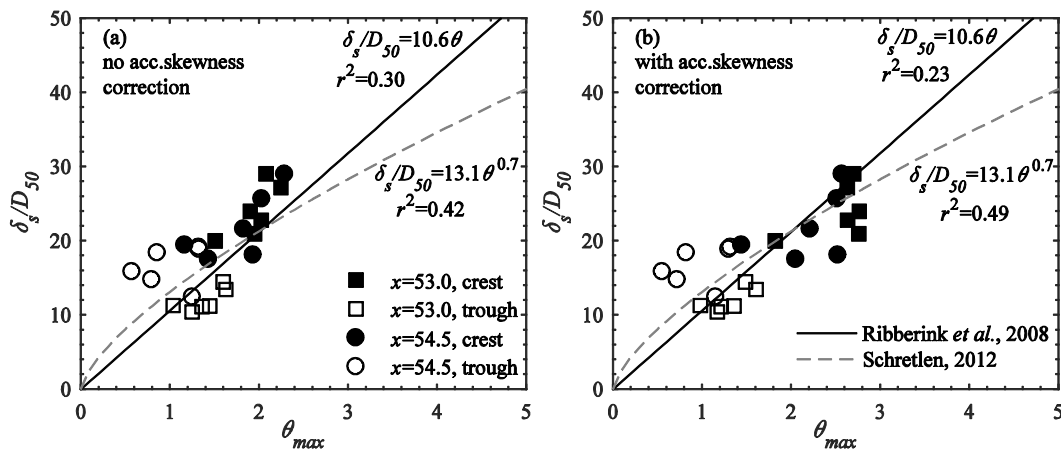
$$481 \quad f_w = 0.00251 \exp \left[5.21 \left(2 \frac{T_a}{T_{hc}} \right)^{-0.49} \left(\frac{a}{k_{sw}} \right)^{-0.19} \right] \quad (7),$$

482 with k_{sw} being the bed roughness, calculated iteratively as a function of the Shields parameter (see
 483 Ribberink, 1998). The parameter T_a/T_{hc} is the relative time duration of accelerating flow within a half-
 484 cycle, which can be used to account for acceleration skewness effects on the bed shear stress (da Silva *et*
 485 *al.*, 2006; van der A *et al.*, 2013). In the present study, T_a/T_{hc} equals approximately 0.3 during the crest

486 phase and 0.6 during the trough phase. This yields friction factors f_w that are approximately 30% higher for
 487 the crest phase and approximately 6% lower for the trough phase compared to f_w calculated without
 488 acceleration-skewness correction (i.e. $T_a = 0.5$ in Equation 7). The maximum bed shear θ_{max} and sheet flow
 489 thickness δ_s are derived per half cycle and for each 15-minute stage of bar development, yielding a total of
 490 24 data points. For the D_{50} , a constant value of 0.25 mm (from sieving tests) was used for all runs. Using
 491 the locally measured D_{50} at the end of the experiment (by laser-diffraction particle sizer) in the calculations
 492 would result in θ_{max} values that are 10 to 20% higher.

493 **Figure 7** shows measured δ_s versus θ_{max} , for θ calculations without (panel a) and with (panel b) acceleration
 494 skewness corrections. The measured data cluster around the predictions by Equations 5 and 6. This suggests
 495 that δ_s in the present breaking-wave conditions is consistent with previous observations in oscillatory flow
 496 tunnel and non-breaking wave conditions, despite effects of the sloping bed, the presence of breaking-
 497 generated turbulence in the WBL, and the non-uniformity of the flow. Without acceleration skewness
 498 correction, the measured crest-phase δ_s values tend to be slightly higher than the empirical predictions
 499 (**Figure 7a**). When acceleration skewness effects are corrected for through T_a/T_{hc} in Equation (7), the
 500 estimated crest-phase θ increases while the trough-phase θ decreases. In that case, the agreement between
 501 measured and predicted δ_s decreases for Equation 5 (from $r^2 = 0.30$ to 0.23) but increases for Equation 6
 502 (from $r^2 = 0.42$ to 0.49).

503



504

505 Figure 7. Maximum sheet flow layer thickness versus maximum Shields stress per wave half-cycle,
 506 without (a) and with (b) acceleration skewness correction in calculations of θ . Also included are empirical
 507 relations proposed by Ribberink *et al.*, 2008 (Eq. 5; solid line) and Schretlen, 2012 (Eq. 6; dashed line).

508

509 4.3 Sheet flow particle velocities and fluxes

510 Particle velocities $u_p(\zeta)$ across the sheet flow layer were estimated for CCM⁺ tank 1 at $x = 54.5$ m through
 511 cross-correlation of concentration measurements by two probes aligned in wave direction (see Section 2.5).
 512 Inherent to the applied CCM cross-correlation technique is that reliable estimates of particle velocities can
 513 only be obtained when the sheet flow layer is well-developed (c.f. Dohmen-Janssen and Hanes, 2002).
 514 Because the sheet flow layer in the present study is rather thin, u_p could only be measured around instances
 515 of maximum onshore/offshore velocity. We focus here on the final run ($t = 75$ – 90 minutes) when near-bed
 516 velocities were highest and the best measurements of u_p were obtained.

517 **Figure 8a** shows phase-averaged particle velocities for $t = 75\text{--}90$ min. Reliable estimates of u_p were
 518 obtained for phases with δ_s roughly exceeding 4 mm. The particle velocities are in phase with near-bed
 519 water velocity and increase in magnitude with distance away from the bed. Magnitudes of u_p are typically
 520 about 40-70% of the near-bed flow velocity at $\zeta = \delta$. These relative magnitudes and the vertical structure
 521 are both consistent with previous observations of oscillatory sheet flows (e.g. McLean *et al.*, 2001;
 522 Dohmen-Janssen and Hanes, 2002; Dohmen-Janssen and Hanes, 2005).

523 The particle velocities were multiplied with corresponding concentrations to obtain horizontal sediment
 524 fluxes ϕ_x (**Figure 8b**). Highest sediment fluxes are found deep in the erosion layer because concentrations
 525 increase rapidly towards the bed while the vertical decay of velocities is much more gradual. Note that flux
 526 magnitudes in the sheet flow layer (100–500 kg/m²s) are orders of magnitude higher than horizontal
 527 suspended sediment fluxes measured just above the WBL at the same location (1–10 kg/m²s) (van der
 528 Zanden *et al.*, 2017).

529 The time-varying total transport $q_{sfl}(t)$ was estimated as the depth-integrated product of measured
 530 concentrations C and estimated particle velocities u_p over the sheet flow layer, i.e. from the erosion depth
 531 z_e to the top of the upper sheet flow layer z_t :

$$532 \quad q_{sfl}(t) = \int_{z_e}^{z_t} u_p(\zeta, t) C(\zeta, t) d\zeta \quad (8).$$

533 The full $u_p(\zeta, t)$ profile was obtained by fitting an empirical power-law distribution, proposed by Sumer *et*
 534 *al.* (1996), through the measurements:

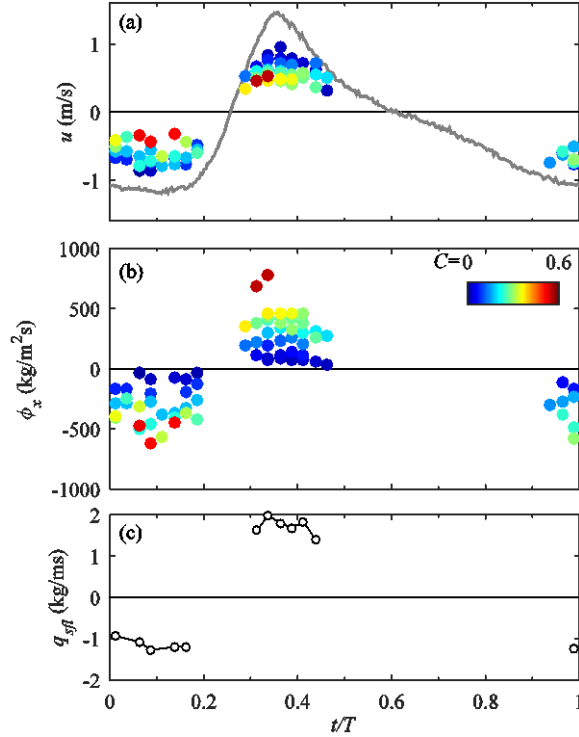
$$535 \quad u_p(\zeta) = m \cdot \zeta^n \quad (9),$$

536 with m and n as fitting parameters. Equation 9 was log-fitted for each phase with a minimum of three $u_p(\zeta)$
 537 measurements and accepted only if $n > 0$, yielding fitted $u_p(\zeta)$ profiles for 12 out of 40 wave instants with
 538 an average $r^2 = 0.62$. The accordingly obtained velocity distributions may not be fully correct but are
 539 considered sufficiently accurate for estimating the magnitude of $q_{sfl}(t)$.

540 Results of $q_{sfl}(t)$ in **Figure 8c** show that instantaneous transport rates during the crest phase exceed those
 541 during the trough phase with about 50%. This is consistent with δ_s being larger during the crest phase.
 542 Indeed, **Figure 8b** shows that sediment fluxes associated with a particular concentration are of similar
 543 magnitude during trough and crest phase. Hence, the vertical profile of horizontal fluxes is of similar shape
 544 during both crest and trough phase, and the larger sheet flow thickness during the crest phase leads to flux
 545 profiles that are vertically stretched and yield larger transport rates. It is further interesting to note that $q_{sfl}(t)$
 546 is of $O(1\text{--}2 \text{ kg/ms})$, which is of similar magnitude as the depth-integrated outer-flow suspended load
 547 transport $q_s(t)$ at this location (approximately 2.0 (+/- 0.2) kg/ms, van der Zanden *et al.*, 2017).

548 Averaging $q_{sfl}(t)$ over the wave period yields a rough approximation of the time-averaged transport in the
 549 sheet flow layer $\overline{q_{sfl}}$, excluding transport contributions around flow reversals when u_p could not be
 550 measured. Estimated $\overline{q_{sfl}} = 0.03$ (+/- 0.1) kg/ms, i.e. the net transport over a wave cycle is two orders of
 551 magnitude lower than the instantaneous transport rate during the half cycles.

552



553

554 Figure 8. Sheet flow particle velocities and sediment fluxes measured with CCM⁺ at $x = 54.5$ m, for $t =$
 555 75-90 min. (a) ACVP-measured velocities at $\zeta = \delta$ (line) and particle velocities measured with CCM⁺ for
 556 eight concentration bin classes (circles, with color coding indicating the volumetric concentration, see
 557 color bar in panel b); (b) Flux measurements, as product of CCM⁺-measured particle velocities and
 558 concentrations; (c) Time-varying depth-integrated transport over the sheet-flow layer.

559

560 4.4 Net bedload transport rates

561 The total net (i.e. wave-averaged) transport rate q_{tot} is formed by a depth-integrated suspended load (q_s) and
 562 a bedload (q_{bed}) contribution. Direct measurement of q_{bed} in oscillatory conditions is generally very difficult,
 563 because the transport is confined to layers of $O(\text{sub-mm})$ which cannot be accurately resolved by most
 564 measuring instruments. The CCM⁺ is one of the few instruments capable of measuring q_{bed} in sheet flow
 565 conditions, provided that sheet flow layers are sufficiently developed ($\delta_s > 4$ mm). Most previous laboratory
 566 studies focusing on bedload transport rates could assume negligible suspended load transport (i.e. $q_{bed} \approx$
 567 q_{tot}), allowing quantification of q_{bed} from bed profile measurements (i.e. through Equation 3). However,
 568 because the breaking waves in the present study bring large amounts of sediment into suspension, q_s cannot
 569 be neglected. Following previous surf zone studies (Grasmeijer and Van Rijn, 1997; van der Werf *et al.*,
 570 2015), q_{bed} is estimated at each location as the difference between the measured total transport (Equation 3)
 571 and the measured suspended transport rates:

$$572 \quad q_{bed}(x) = q_{tot}(x) - q_s(x) = q_{tot}(x) - \int_{z_a}^{\eta_{crest}} \overline{u(x, \zeta) C(x, \zeta)} d\zeta \quad (10).$$

573 The net suspended transport rate q_s is the time-averaged cross-shore sediment flux, depth-integrated from
 574 a near-bed reference elevation z_a that defines the boundary between the bedload layer ($\zeta < z_a$) and the
 575 suspension layer ($\zeta > z_a$) up to wave crest level η_{crest} . The reference elevation $z_a = 0.005$ m, which roughly

576 equals the maximum elevation of the sheet flow layer across the test section. Between $\zeta = z_a$ and 0.10 m,
 577 the ACVP measured the instantaneous flux through collocated u and C , enabling direct quantification of
 578 the net total flux \overline{uC} including contributions of the wave-related flux $\overline{\tilde{u}\tilde{C}}$ and the turbulent diffusive flux
 579 $\overline{u'C'}$. The latter is resolved up to a 5 Hz frequency, hence capturing the contributions by the largest vortices
 580 that likely contribute most to net diffusion. For the present experiment, contributions of $\overline{\tilde{u}\tilde{C}}$ and $\overline{u'C'}$ were
 581 generally only significant inside the wave bottom boundary layer ($\zeta < \delta \approx 0.02$ m); at outer-flow elevations
 582 ($\zeta > \delta$) the net total flux was almost fully due to the current-related contribution, i.e. $\overline{uC} \approx \overline{u}\overline{C}$. Therefore,
 583 for $\zeta > 0.10$ m, the net flux was estimated based on inter- and extrapolated vertical profiles of the time-
 584 averaged velocity (ADV measurements) and sand concentration (TSS measurements). More details on the
 585 calculation of q_s are given by van der Zanden *et al.* (2017).

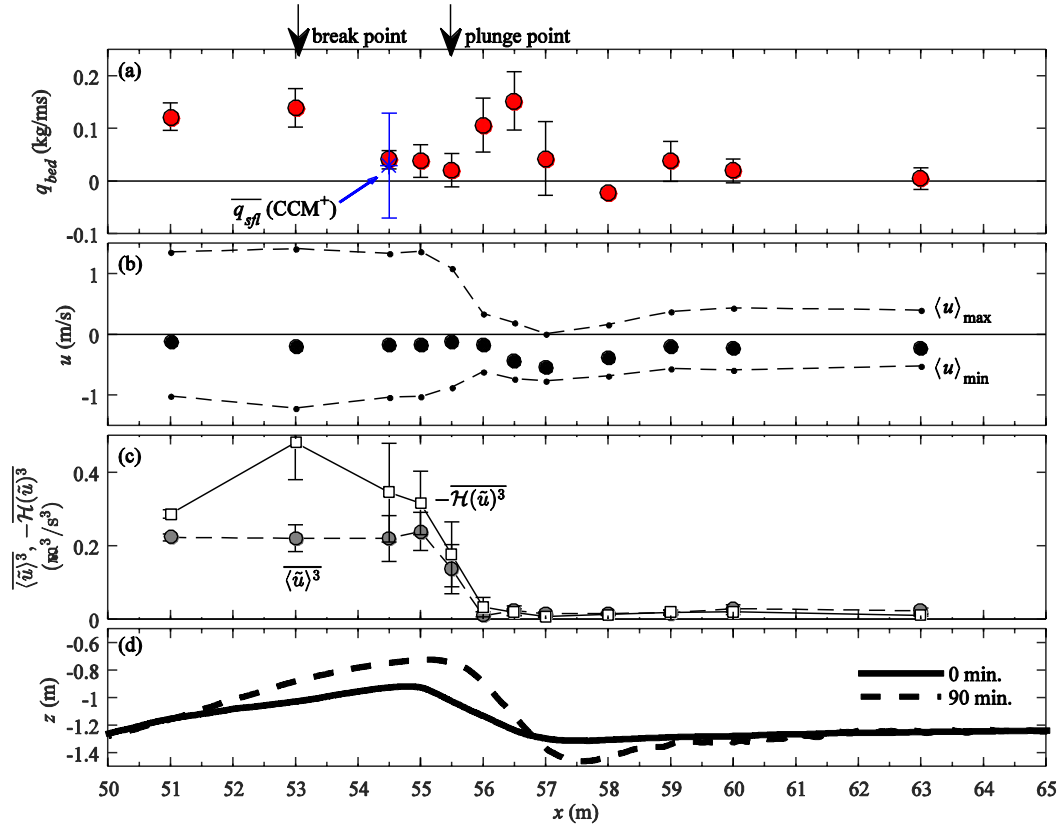
586 The possible sources of measurement errors for q_s and q_{bed} are addressed in Section 7 (Discussion). Based
 587 on the variability between measurements taken at the same location but for six different runs, the
 588 measurement uncertainties of q_s and q_{bed} transport were both estimated as 0.04 kg/ms = $1.5 \cdot 10^{-5}$ m²/s on
 589 average. These estimates include the variability due to the morphologic feedback by the bed profile
 590 evolution on the transport rates during the experiment.

591 **Figure 9a** presents q_{bed} across the breaker bar. The figure includes the time-averaged sheet flow layer
 592 transport measured with the CCM⁺, $\overline{q_{sfl}} = 0.03$ kg/ms. Note the wide error margins (+/- 0.1 kg/ms) of this
 593 measurement, which illustrate the difficulties of obtaining direct measurements of bedload transport rates.
 594 At this location, Equation 10 yields $q_{bed} = 0.07$ (+/- 0.04) kg/ms, which is close to the estimated $\overline{q_{sfl}}$ and
 595 within the latter's error margins. The bedload transport rates (**Figure 9a**) can be explained in terms of
 596 hydrodynamic parameters, i.e. the onshore and offshore phase-averaged velocity (**Figure 9b**), the
 597 dimensional periodic velocity skewness $\overline{\langle \tilde{u} \rangle^3}$, and the dimensional acceleration skewness $-Hu(\langle \tilde{u} \rangle^3)$ (where
 598 H is the Hilbert transform, see e.g. Elgar, 1987; Henderson *et al.*, 2004) (**Figure 9c**).

599 At $x = 51.0$ m, q_{bed} is positive (i.e. onshore), which is explained by the strong velocity- and acceleration-
 600 skewness of near-bed velocities and the relatively low magnitude of time-averaged undertow velocities
 601 (**Table 2**). Note that this location corresponds roughly to the location of maximum q_{tot} as obtained from bed
 602 profile measurements (**Figure 5**). Magnitudes of q_{bed} are similar at $x = 53.0$ m (below break point), where
 603 the dimensional acceleration skewness is maximum. Towards the bar crest ($x = 54.5$ – 55.0 m), q_{bed}
 604 decreases, which may be caused by the decrease in acceleration skewness (compared to $x = 53.0$ m) and the
 605 increase in offshore-directed undertow magnitude (compared to $x = 51.0$ m).

606 Shoreward from the plunge point and along the lee-side slope of the bar, q_{bed} increases significantly. Note
 607 that $q_{bed} > 0$ while near-bed velocities are predominantly negative. Hence, the onshore transport is likely
 608 due to the large steepness of the bar, which approaches the natural angle of repose and induces downward
 609 (onshore) bedload transport by gravity. The transported grains partly accumulate at the steep offshore-
 610 facing front of the bed forms at this region, which contributes to the progressive offshore migration of these
 611 bed forms across the bar slope (see Section 3.2). The breaker trough ($x = 58.0$ m) is the only location where
 612 q_{bed} is directed offshore. This is explained by the combination of the positive bed slope dz_{bed}/dx and the
 613 strong offshore-directed undertow velocities relative to periodic velocities. Further shoreward, at the inner
 614 surf zone ($x = 59.0$ – 63.0 m), q_{bed} is again shoreward-directed with magnitudes gradually approaching zero.

615



616

617 Figure 9. Bedload transport rates across the bed profile. (a) q_{bed} , mean (circles) plus 95% confidence
 618 interval (error bars) over six runs per location. Also included is the time-averaged sheet flow transport
 619 measured with CCM⁺ at $x = 54.5$ m for $t = 75$ –90 min. (star symbol, with error bars indicating the
 620 estimated error = +/- 0.1 kg/ms); (b) Horizontal velocity at the WBL overshoot elevation, time-averaged
 621 (black circles) and maximum onshore and offshore phase-averaged (dots and dashed lines) for $t = 0$ –90
 622 min; (c) Dimensional velocity skewness (circles) and dimensional acceleration skewness (squares) at the
 623 WBL overshoot elevation, mean values over six runs plus 95% confidence interval (error bars); (d) Bed
 624 profiles at start (solid) and end (dashed) of experiment.

625

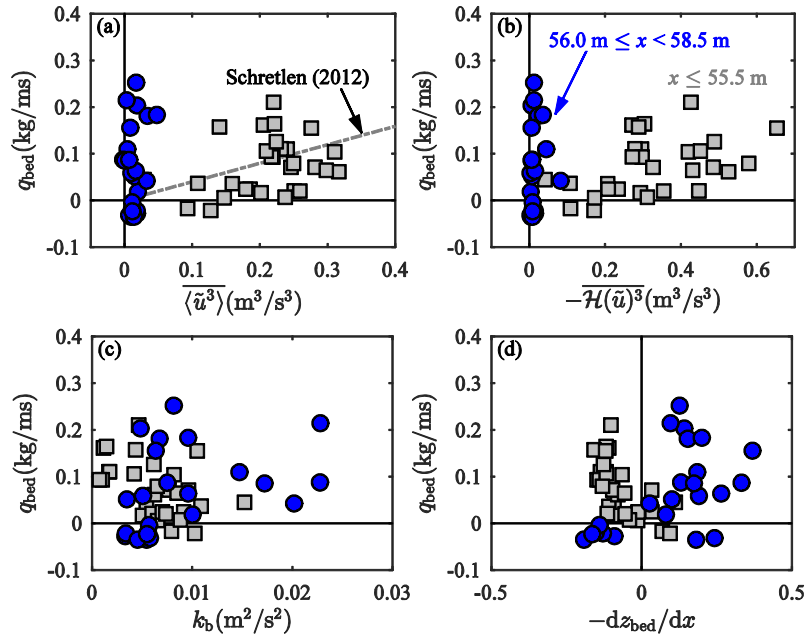
626 In order to obtain more insight in the parameters controlling the measured bedload transport rates, **Figure**
 627 **10** shows scatter plots of q_{bed} versus a number of hydrodynamic parameters. The chosen parameters are the
 628 dimensional orbital velocity skewness, $\overline{\langle \tilde{u} \rangle^3}$ (**Figure 10a**); the dimensional acceleration skewness, $-\overline{Hu(\langle \tilde{u} \rangle^3)}$
 629 (**Figure 10b**); the near-bed turbulent kinetic energy k_b (**Figure 10c**); and the local bed slope $-dz_{bed}/dx$
 630 (**Figure 10d**). Distinction is made between two characteristic zones along the test section, i.e. the offshore
 631 slope up to the bar crest ($x \leq 55.5$ m) and the breaking region covering the bar crest up to the bar trough
 632 ($55.5 < x < 58.5$ m). The bedload transport rates in the inner surf zone are not considered in this analysis
 633 because of the presence of bed forms and the associated variability in bed roughness. In what follows,
 634 coefficients of determination (r^2) are calculated based on a linear regression between the two considered
 635 parameters.

636 For medium-sand and plane-bed conditions, q_{bed} is expected to correlate positively with the degree of orbital
 637 velocity skewness. **Figure 10a** shows q_{bed} versus $\overline{\langle \tilde{u} \rangle^3}$ and includes a linear trend line that was found by
 638 Schretlen (2012) for medium sand ($D_{50} = 0.25$ mm) under non-breaking second-order Stokes waves.
 639 Between $x = 51.0$ and 55.5 m, measured q_{bed} in the present study is of similar magnitude as the observations
 640 for non-breaking waves by Schretlen (2012). The scatter in measured q_{bed} is addressed to measuring
 641 uncertainties and to effects by other hydrodynamic parameters than $\overline{\langle \tilde{u} \rangle^3}$. The transport rates along the
 642 shoreward bar slope (between $x = 56.0$ and 58.5 m) deviate clearly from the trend line, suggesting that other
 643 forcing parameters than $\overline{\langle \tilde{u} \rangle^3}$ are significant at these cross-shore locations.

644 A positive correlation between q_{bed} and the dimensional acceleration skewness is expected based on
 645 previous sheet flow transport measurements (c.f. van der A *et al.*, 2010). **Figure 10b** shows that between x
 646 $= 51.0$ and 55.5 m, q_{bed} indeed correlates positively with $-\overline{H(\langle \tilde{u} \rangle^3)}$. However, the data points in the breaking
 647 region along the shoreward bar slope ($x = 56.0$ to 58.5 m) do not satisfy the overall trend.

648 As shown by Sumer *et al.* (2003), an increase in near-bed TKE can lead to increased q_{bed} magnitudes.
 649 Therefore, **Figure 10c** shows the scatter of q_{bed} versus the turbulent kinetic energy inside the WBL, k_b . The
 650 figure indeed suggests a positive relation between q_{bed} and k_b in the wave breaking region between $x = 56.0$
 651 and 58.5 m, but the correlation is weak ($r^2 = 0.13$; significant at $P < 0.10$ but not at $P < 0.05$).

652



653
 654 Figure 10. Scatter plot between bedload transport and near-bed hydrodynamic parameters for 6 runs at 12
 655 cross-shore locations (72 data points). Explaining parameters are (a) periodic velocity cubed; (b)
 656 dimensional acceleration skewness through Hilbert transform $-\overline{H(\langle \tilde{u} \rangle^3)}$; (c) time-averaged TKE in WBL;
 657 (d) local bed slope. Velocity variables (a-b) are obtained at overshoot elevation $\zeta = \delta$. Distinction is made
 658 between measurements along offshore bar slope to bar crest ($x \leq 55.5$ m; squares) and between bar crest
 659 and bar trough ($56.0 \leq x < 58.5$ m; circles).

660

661 Gravity favors downslope bedload transport, i.e. a positive relation between q_{bed} and $-dz_{bed}/dx$ is expected.
 662 **Figure 10d** indeed shows a positive correlation ($r^2 = 0.24$; significant at $P < 0.05$) between both variables
 663 for the observations between bar crest and bar trough ($x = 56.0$ to 58.5 m). This region involves the locations
 664 along the shoreward-facing bar slope, where particularly steep local bed slopes with a substantial effect on
 665 bedload transport are found. Note that although the locations between $x = 56.0$ and 58.5 m are characterized
 666 by simultaneously high $-dz_{bed}/dx$ and k_b , these two forcing parameters did not reveal significant correlation
 667 ($r^2 = 0.04$; $P < 0.10$) for this subset of measurements, suggesting that both parameters are statistically
 668 independent. **Figure 10d** also reveals a negative relation between $-dz_{bed}/dx$ and q_{bed} for the locations
 669 offshore from the bar crest ($x \leq 55.5$ m) (significant at $P < 0.05$). This suggests that onshore bedload
 670 transport increases for steeper shoreward-tilted bed slopes, which is physically unlikely. The positive
 671 correlation between $-dz_{bed}/dx$ and q_{bed} is instead explained by positive covariance between $-dz_{bed}/dx$ and the
 672 aforementioned forcing parameters $\overline{\langle \tilde{u} \rangle^3}$ and $-Hu(\langle \tilde{u} \rangle)^3$ ($r^2 = 0.25$ and 0.29 , respectively; both significant at
 673 $P < 0.05$).

674

675 **5. Contributions of transport components to bar morphodynamics**

676 **5.1 Bedload and suspended load contributions to total transport**

677 **Figure 11a** shows the cross-shore variation of the net (i.e. wave-averaged) bedload ($\zeta < z_a = 0.005$ m) and
 678 the net depth-integrated suspended load ($\zeta > z_a$) transport rates. The net suspended load transport is further
 679 decomposed into a current-related ($q_{s,c}$) and wave-related component ($q_{s,w}$). The latter was measured with
 680 ACVP, and was generally confined to the WBL and onshore-directed (van der Zanden *et al.*, 2017). **Figure**
 681 **11b** shows the relative importance f_{rel} of these three components to total transport, calculated as the relative
 682 contribution to the sum of the absolute value of individual components (e.g. for bedload, $f_{rel} = |q_{bed}| / (|q_{bed}|$
 683 $+ |q_{s,c}| + |q_{s,w}|)$).

684 At the most offshore shoaling location ($x = 51.0$ m), transport is almost fully (>90%) attributed to bedload.
 685 This location is hardly affected by breaking-generated TKE and suspended sediment pick-up rates are low.
 686 Towards the crest of the bar, between the break point ($x = 53.0$ m) and plunge point ($x = 55.5$ m), the
 687 offshore-directed suspended transport gains importance over bedload transport, i.e. q_s increases while q_{bed}
 688 decreases. At these locations the onshore-directed wave-related suspended load contribution ($f_{rel} = 10$ – 20%)
 689 is also significant.

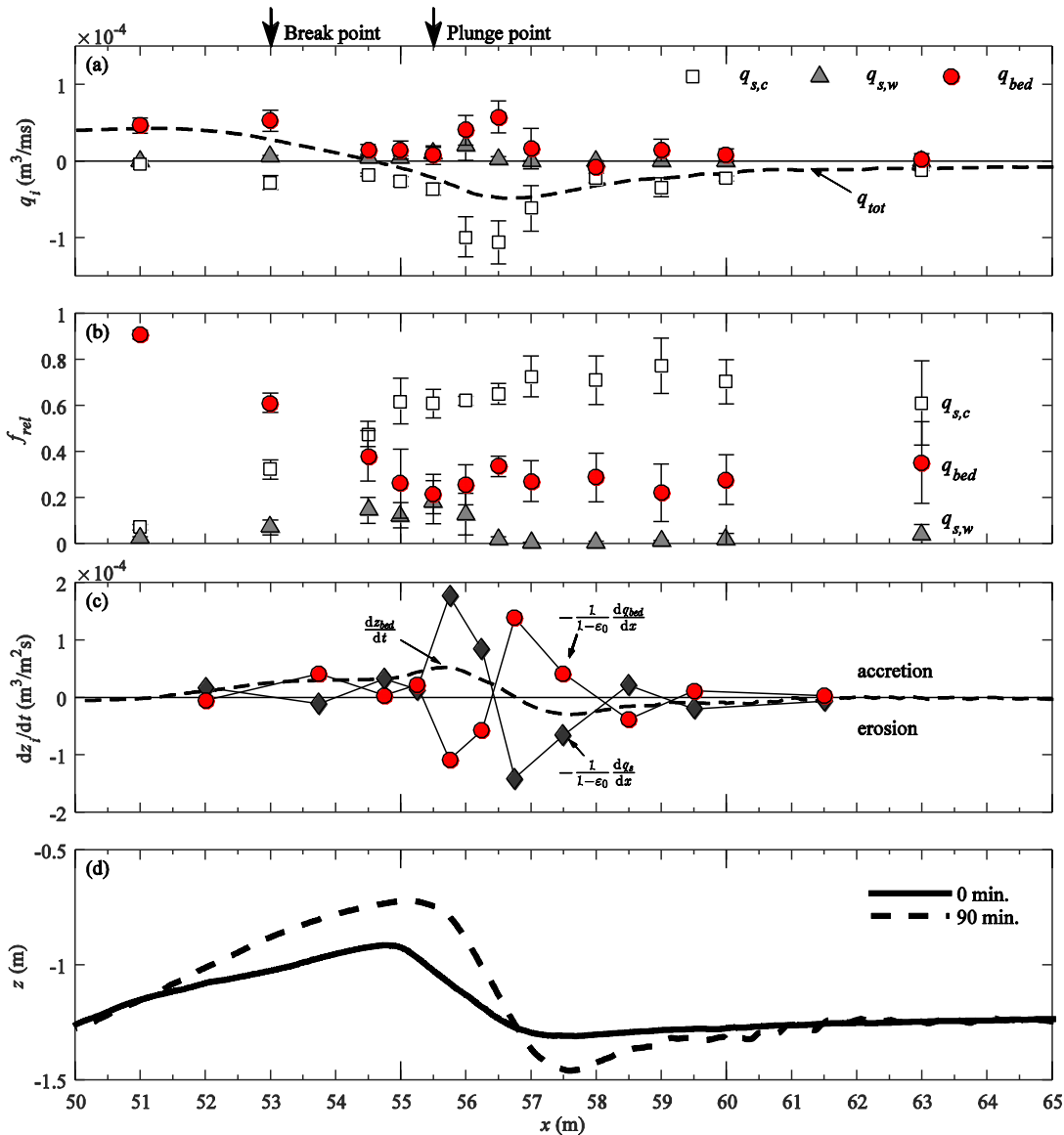
690 Along the lee side of the bar and shoreward from the plunge point ($x = 56.0$ – 57.0 m), both q_s and q_{bed}
 691 increase in magnitude. Magnitudes of offshore-directed q_s exceed those of onshore-directed q_{bed} by about a
 692 factor 2 ($f_{rel} \approx 0.7$ for q_s ; $f_{rel} \approx 0.3$ for q_{bed}). The physical explanations for the increase in both transport
 693 components are notably different: q_s increases due to the combination of strong near-bed undertow
 694 velocities and enhanced sediment pick-up by breaking-generated turbulence, while q_{bed} increases primarily
 695 due to bed slope effects. Further shoreward at bar trough and inner surf zone locations ($x \geq 58.0$ m), both
 696 transport components decrease in magnitude and the established relative contributions by q_s ($f_{rel} \approx 0.7$) and
 697 q_{bed} ($f_{rel} \approx 0.3$) remain approximately constant.

698

699 **5.2 Bedload and suspended load transport contributions to breaker bar development**

700 **Figure 11c** shows the negative cross-shore gradients ($-d/dx$) of q_s and q_{bed} , divided by the sediment fraction
 701 in a loosely packed bed ($1 - \varepsilon_0$; with porosity $\varepsilon_0 = 0.4$). These terms can be interpreted as the contributions
 702 by both transport components to local bed level changes. The signs are chosen such that positive values
 703 correspond to net local accretion, and negative values to net erosion, of the bed.

704 Suspended transport leads to erosion of the bar trough ($x = 56.5 - 58.0$ m) and accretion of the bar crest and
 705 higher ends of the shoreward bar slope ($x = 54.0 - 56.5$ m). Bedload transport leads to accretion of the
 706 breaker bar ($x = 52.0 - 55.5$ m), erosion of the shoreward bar slope ($x = 55.5 - 56.5$ m) and accretion of the
 707 breaker trough ($x = 56.5 - 58.0$ m). Hence, the net bed level change between $x = 55.0$ and 58.0 m (bar crest
 708 to bar trough) is explained by the net difference between opposite contributions by suspended load and
 709 bedload. Suspended load transport contributions to the bar morphodynamics exceed those by bedload,
 710 which explains the growth of the bar crest and deepening of the bar trough during the experiment.



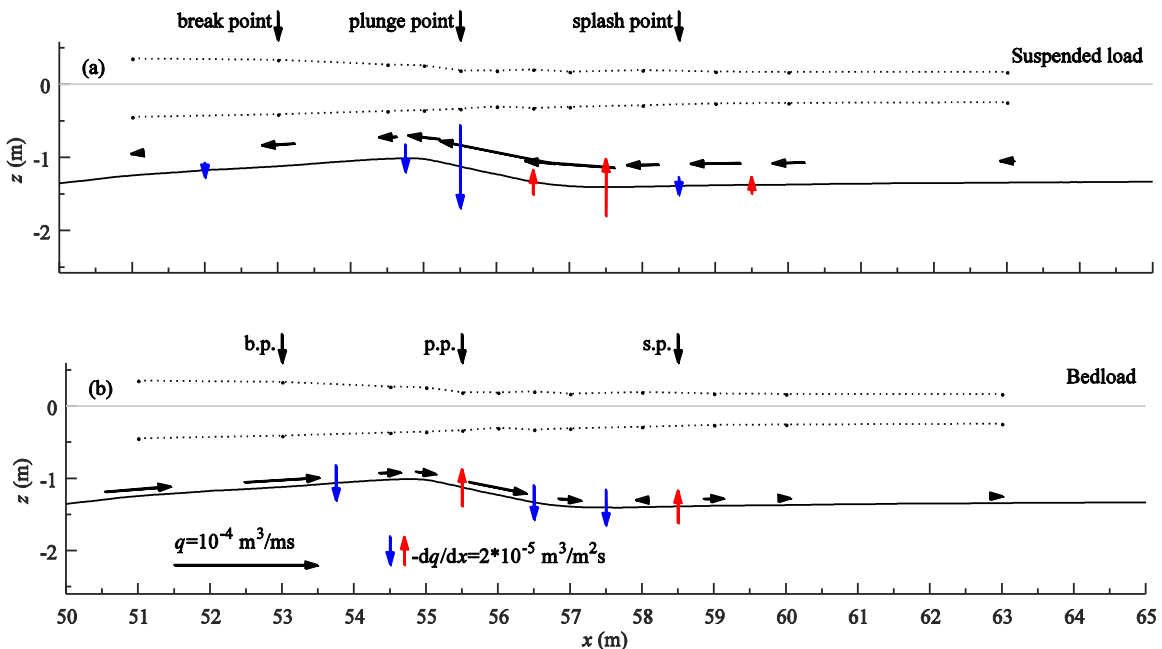
711
 712 Figure 11. Cross-shore variation in net (wave-averaged) transport rates. (a) Net transport rates along test
 713 section: total transport (dashed black line), current-related suspended transport (squares), wave-related
 714 suspended transport (triangles), and bedload (circles); (b) Relative contribution of each component to total
 715 transport, calculated as individual contribution to the sum of absolute values of the three terms (see text in

716 Section 5.1); (c) Contributions by each component to bed level change (erosion/accretion), quantified
 717 through horizontal transport gradients divided by relative sand fraction in loosely packed bed ($1 - \epsilon_0$):
 718 contributions by suspended load (wave- plus current-related, diamonds), bedload (circles) and total
 719 transport (dashed line); (d) Bed profiles at $t = 0$ and 90 min. Values in (a-c) are means over six runs, with
 720 error bars in a-b marking 95% confidence interval.

721
 722 **Figure 12** shows the suspended load (panel a) and bedload (panel b) transport rates again, but this time as
 723 a vector plot along the bar profile and in combination with their effects on local bed level changes. The
 724 figure illustrates how sediment advection occurs as suspended and bed load in opposite directions, and how
 725 both components lead to local bed erosion or accretion. Suspended transport particularly reveals net
 726 sediment pick-up in the bar trough. Once entrained, suspended grains are advected offshore and upwards
 727 along the shoreward slope of the breaker bar by the undertow. The offshore-directed suspended transport
 728 increases in offshore direction along the shoreward slope of the bar, due to the concurrent strong undertow
 729 and enhanced entrainment by breaking-generated TKE (van der Zanden *et al.*, 2017). Suspended sediment
 730 is deposited at the bar crest where both undertow magnitudes and TKE levels decrease (compared to
 731 shoreward locations).

732 Bedload transport rates are large at shoaling locations ($x = 51.0$ and 53.0 m) and reduce towards the breaker
 733 bar. This leads to net sediment deposition by bedload transport between the break point and the bar crest (x
 734 $= 53.0 - 54.5$ m). Bedload transport rates increase along the lee-side slope of the bar, due to the steep bed
 735 slope and possibly because of increased near-bed TKE levels. It is also possible that the high q_{bed} at $x \approx 56.0$
 736 m is partly due to the vertical influx by net settling of suspended grains at $x = 55.0 - 56.0$ m (**Figure 12a**);
 737 these grains are already mobilized and are likely to be transported (as bedload) more easily than the grains
 738 contained in the bed. The bedload transport between $x = 55.0$ and 57.5 m leads to erosion of the bar crest
 739 and accretion of the bar trough (**Figure 12b**) and counterbalances a large part of the bar accretion induced
 740 by the suspended sediment transport (**Figure 12a**).

741



742

743 Figure 12. Vector plot of transport rates and transport gradients, time-averaged over $t = 0$ -90 min, of
 744 depth-integrated suspended load (panel a) and bedload (panel b) transport. Bed-parallel arrows (black)
 745 denote cross-shore transport rates, consistent with Figure 11a. Vertical arrows are cross-shore gradients of
 746 each transport component, with red (upward) indicating a positive gradient dq/dx (corresponding to local
 747 erosion) and blue (downward) corresponding to negative dq/dx (local accretion). The bed profile (solid
 748 black line) is at $t = 0$ min. Transport gradients with magnitudes $< 1.0 \cdot 10^{-5} \text{ m}^3/\text{m}^2\text{s}$ were truncated for
 749 illustration purposes.

750

751 6. Grain-size sorting

752 This section examines the vertical grain-size sorting in suspended sediment (Section 6.1) and the cross-
 753 shore sorting along the bed surface of the breaker bar (Section 6.2). The latter is related to size-selective
 754 transport as bedload and suspended load.

755 6.1 Vertical sorting of suspended sediment

756 **Figure 13** shows vertical profiles of the median diameter (D_{50}) of suspended sediment, sampled with a six-
 757 nozzle Transverse Suction System (TSS). Profiles of D_{10} and D_{90} are qualitatively similar and are not shown
 758 here for brevity. Different behavior is observed for locations relatively far offshore/shoreward from the
 759 plunge point, i.e. at the shoaling location $x = 51.0$ m and at inner surf-zone locations $x = 59.0$ – 63.0 m,
 760 versus the locations in the breaking region ($x = 53.0$ – 58.0 m).

761 At the shoaling and inner surf zone, it is firstly shown that the D_{50} of particles in suspension is substantially
 762 lower than the mean D_{50} in the flume (grey line). Secondly, vertical sorting occurs, as the suspended
 763 sediment becomes finer with distance from the bed. At inner surf zone locations ($x > 58.5$ m), the D_{50} at the
 764 highest TSS nozzle ($\zeta=0.53$ m) is systematically larger than the D_{50} measured closer to the bed (at $\zeta=0.31$
 765 m). A possible explanation is that the sand fraction at $\zeta=0.53$ m contains a larger fraction of sediment that
 766 is entrained in the breaking region and then advected to the inner surf zone at elevations above wave trough
 767 level (see van der Zanden *et al.*, 2017). Similarly, the suspended sediment at $x = 51.0$ m is not necessarily
 768 entrained locally, but may instead consist of the finest fractions of sediment particles that are picked up in
 769 the breaking region and then advected offshore.

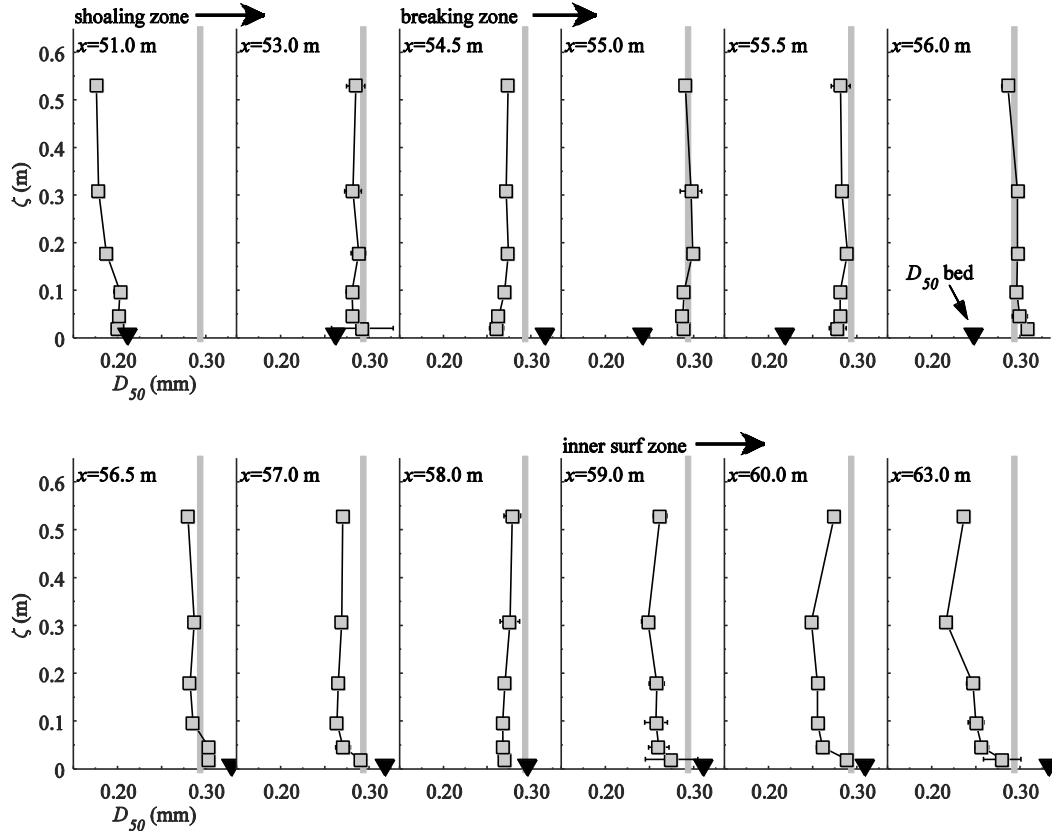
770 In the breaking region ($x = 54.5$ to 58.0 m), large suspended sediment concentrations were found up to the
 771 water surface due to large pick-up rates and strong vertical mixing (van der Zanden *et al.*, 2017). **Figure**
 772 **13** shows little vertical segregation in D_{50} for this region, especially for the locations ± 1 m from the
 773 plunge point (at $x = 55.5$ m). The suspended sediment appears to be well-mixed and also the coarsest
 774 particles are carried to high elevations (up to water surface). Moreover, the D_{50} of suspended sediment is
 775 almost the same as the mean D_{50} of the initial bed.

776 The different sorting behavior for shoaling and inner surf zone versus the breaking region can be related to
 777 the processes responsible for sediment pick-up and vertical mixing. Davies and Thorne (2016) detail how
 778 for vortex-rippled beds, vertical mixing of particles is due to combined convection (by relatively large
 779 coherent periodic vortices ejected from the bed) and diffusion (by random turbulent fluctuations).
 780 Convection becomes increasingly important in terms of sediment entrainment and mixing for the coarser
 781 fractions in a sediment mixture (Davies and Thorne, 2016). At the shoaling and inner surf zone, turbulent
 782 vortices are primarily bed-generated and have a relatively small time and length scale. These small vortices
 783 lead to size-selective pick-up and also to vertical segregation of suspended sediment due to differences in
 784 vertical mixing and settling for each sediment size fraction, as shown for sheet flow conditions in an
 785 oscillatory flow tunnel (Hassan, 2003) and for rippled beds under uniform non-breaking waves (Sisternans,
 786 2002; Davies and Thorne, 2016). In the wave breaking region, turbulent vortices are of larger scale and are

787 more energetic, i.e. have a strong convective mixing capacity for a broad particle size range. Consequently,
 788 vertical sorting in suspended sediment particle size is restricted under breaking waves (see also Wang *et*
 789 *al.*, 1998).

790

791



792

793 Figure 13. Vertical profiles of median diameter (D_{50}) of suspended sediment particles at the 12
 794 measurement locations. Markers denote means (squares) and 95% confidence interval (horizontal error
 795 bars) over six runs ($t = 0-90$ min.). Black triangles denote the measured D_{50} of the bed at the end of the
 796 experiment ($t = 90$ min.). Vertical grey lines denote the mean D_{50} of the original bed.

797

798 **6.2 Cross-shore sorting in the bed**

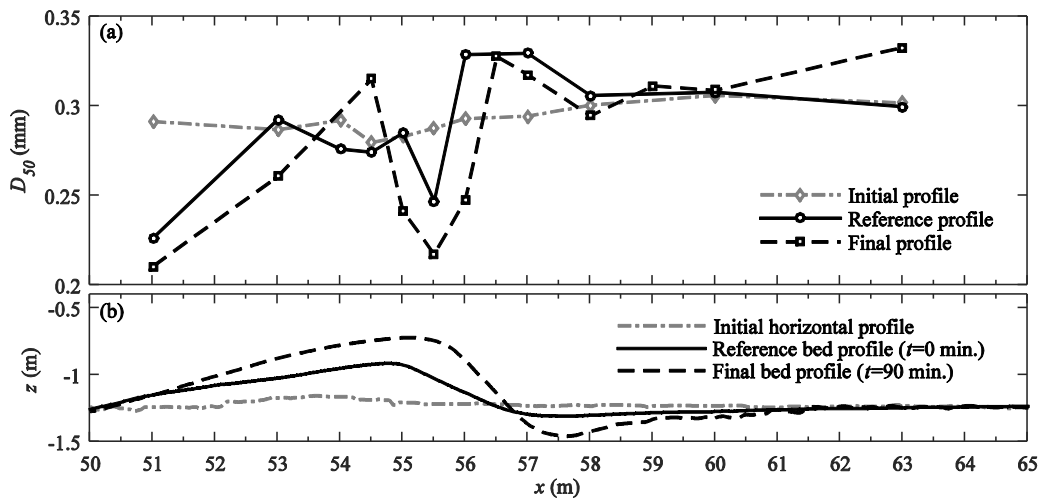
799 **Figure 14** shows the cross-shore variation in D_{50} of bed samples for three stages of bar development.
 800 Starting with an almost homogeneous grain-size distribution along the test section, evident size-sorting
 801 occurs throughout the experiment, resulting in a distinct pattern of grain distribution at the end of the
 802 experiment.

803 At the locations along the offshore slope of the bar ($x = 51.0$ to 54.0 m), the D_{50} decreases in time.
 804 Considering the bedload and suspended load transport patterns (as discussed in the previous sections), the
 805 temporal evolution in D_{50} can be related to two processes: first, net removal of the coarsest grains in the
 806 mixture through selective sheet flow transport (de Meijer *et al.*, 2002; Hassan and Ribberink, 2005); second,
 807 the net deposition of fine suspended particles that are advected offshore from the inner surf and breaking

808 zone, particularly by the undertow (c.f. Sistermans, 2002). The second process (offshore transport of fine
 809 particles) also explains the measured coarsening of the bed at inner surf zone locations ($x > 58.5$ m). This
 810 leads to an overall trend of increasing D_{50} from shoaling to inner surf zone.

811 The region around the breaker bar does not obey this overall trend; additional sorting mechanisms seem
 812 relevant. Slightly offshore from the bar crest (at $x = 54.5$ m) the D_{50} increases, which can be related to the
 813 transport of relatively coarse particles as sheet flow, which are deposited at the bar crest (see also **Figure**
 814 **12**). Slightly shoreward, at the bar crest and the highest elevations along the bar lee side ($x = 55.0 - 56.0$
 815 m), the diameter decreases. Net deposition of suspended grains occurs at these locations (see **Figure 12**).
 816 However, at these locations the grain size of suspended particles is significantly coarser than the particles
 817 forming the bed (**Figure 13**) and consequently, this deposition cannot explain the decreasing D_{50} in the bed.
 818 Instead, it is explained by the gravity-driven bedload transport along the steep lee-side of the breaker bar
 819 (**Figure 12**). Coarser grains in a sediment mixture have a larger tendency to be transported downslope than
 820 finer grains (lee-side sorting). This downslope coarsening along slopes has been shown by several studies
 821 in steady flow conditions (see Kleinhans, 2004, for an overview). The relatively coarse sediment at the
 822 breaker trough ($x = 56.5 - 58.0$ m) supports this explanation.

823



824

825

826 Figure 14. (a) D_{50} sand bed (top 1 to 2 cm) during three stages of bed profile evolution: start of the
 827 experiment with horizontal test section (dot-dashed grey line); after initial 105-min start-up stage, i.e.
 828 reference bed profile at $t = 0$ min. (solid black line); at the end of the experiment, i.e. final bed profile at t
 829 $= 90$ min (black dashed line). (b) Bed profiles corresponding to three bed development stages in (a).

830

831 7. Discussion

832 The present experiment focuses on an evolving breaker bar under forcing of monochromatic normal-
 833 incident waves. Although this set-up allows study of the sand transport processes driving bar growth in
 834 unprecedented detail, it should be noted that these conditions change from natural beaches where waves are
 835 irregular, flow and sand transport is alongshore non-uniform, and bed profiles are usually closer to a semi-
 836 equilibrium state. In addition, in the present bed configuration the breaker bar and trough were separated
 837 from the sloping beach by an elongated inner surf zone in order to reduce the effects of beach processes on

838 breaker bar morphodynamics. This differs from natural beaches and from laboratory studies with plane
 839 sloping initial beds, where the bar-trough region is often more closely connected to the inner surf and swash
 840 zones. If a plane sloping bed had been used as initial bed configuration, water depths in the inner surf zone
 841 would be shallower, likely resulting in a higher offshore-directed suspended sand flux from the inner surf
 842 zone to the breaker trough region and a reduced erosion rate at the bar trough. Also the offshore slope
 843 affects the breaker bar morphodynamics. In the present experiment, a relatively steep slope ($\tan(\alpha) = 0.10$)
 844 was used, leading to strong wave shoaling. This in return resulted in highly cross-shore non-uniform wave
 845 shape and height in the shoaling region, which promoted the erosion of the offshore slope by bedload
 846 transport. Consequently, for a milder and more dissipative offshore slope, one may expect a reduction in
 847 erosion rates by bedload transport under the shoaling waves. Such a milder slope would also importantly
 848 change the wave breaking process and would alter the overall experimental conditions significantly.

849 Bedload transport rates q_{bed} are obtained indirectly by subtracting the depth-integrated suspended load q_s ,
 850 from the total load q_{tot} that was obtained from the bed profile evolution. Due to propagation of errors in the
 851 measurements and data treatment steps (e.g. direct measurement errors, uncertainty in the acoustic inversion
 852 methodology for ACVP-measured concentrations, uncertainties in z_{bed} and q_{tot} as detailed in Section 2.5,
 853 inter- and extrapolation of concentration and velocity profiles to estimate q_s , assumption of cross-flume
 854 uniform flow), the obtained bedload transport rates are subject to relatively large uncertainties. A
 855 quantitative indication of the random error in q_{bed} (0.04 kg/ms) was obtained by calculating the standard
 856 deviation over six runs at the same cross-shore location (see **Figure 11a**). Unfortunately, these uncertainties
 857 in the estimated bedload transport rates cannot be easily overcome, because direct measurements of bedload
 858 transport rates in such a challenging measurement environment are extremely difficult with existing
 859 instrumentation. Two observations justify the use of the indirectly obtained bedload transport rates: first,
 860 the indirect estimates of q_{bed} are consistent with estimates of the wave-averaged sheet flow layer transport
 861 from CCM⁺ measurements (**Figure 9a**); second, q_{bed} scales similarly to hydrodynamic forcing as previous
 862 transport observations of medium-sand sheet flow transport by Schretlen (2012) (see **Figure 10a**).

863 Bedload transport is defined here as the transport that occurs at $\zeta < 0.005$ m above the undisturbed bed
 864 level. This choice affects some results, for example the absolute bedload transport rate and the ratio between
 865 bedload and suspended load transport, and it requires some reflection. If the reference elevation would be
 866 raised to the WBL overshoot elevation (at $\zeta \approx 0.02$ m), the ratio between bedload and suspended load
 867 transport would not change drastically since most (80 to 90%) of the suspended load transport occurs at
 868 outer-flow elevations above the WBL (van der Zanden *et al.*, 2017). Results will likely be more sensitive
 869 to a decrease in reference elevation, due to the strong vertical concentration gradient inside the sheet flow
 870 layer. Nevertheless, previous medium-sand sheet flow measurements showed that the majority of sheet
 871 flow transport is due to horizontal fluxes in the pick-up layer, i.e. at $\zeta < 0$ (Schretlen, 2012). Consequently,
 872 we do not expect the results to change drastically for other reference elevations (within the range $0 < \zeta <$
 873 0.02 m).

874 The present study quantifies, possibly for the first time, the simultaneous contributions by both transport
 875 components to bed level changes across a large-scale breaker bar, and allows a detailed assessment of the
 876 governing mechanisms for bar formation mentioned in the Introduction (Dyhr-Nielsen and Sorensen, 1970;
 877 Dally and Dean, 1984; Zhang and Sunamura, 1994). The present experiment confirms the importance of
 878 suspended sand transport for bar morphodynamics. Most notably is the high local maximum in offshore-
 879 directed q_s in the breaking region between bar crest and bar trough, which is explained by concurrent high
 880 TKE and undertow magnitudes (van der Zanden *et al.*, 2017). These observations support the numerical
 881 results of Dally and Dean (1984), who found a strong increase in q_s magnitudes in the wave breaking region
 882 due to a simultaneous increase in undertow magnitude and in suspended load, which both scale to cross-

883 shore gradients in the wave energy (flux). The present study further supports the extensive descriptions on
 884 the effects of breaking-generated turbulent vortices on bar morphodynamics by Zhang and Sunamura
 885 (1994).

886 Also consistent with aforementioned bar formation mechanisms (Dyhr-Nielsen and Sorensen, 1970; Dally
 887 and Dean, 1984) is the onshore transport in the shoaling zone. However, in contrast with these studies, the
 888 onshore transport in the present experiment is not explained by near-bed suspended sand fluxes driven by
 889 onshore WBL currents, but instead, is due to bed load transport that is driven by wave skewness and
 890 asymmetry. This confirms earlier wave flume observations that suggested that onshore bed load and
 891 offshore suspended load transport rates are of similar magnitude (Grasmeijer and Van Rijn, 1997; Van der
 892 Werf *et al.*, 2015, using data of Roelvink and Reniers, 1995), and also supports studies highlighting the
 893 importance of wave skewness and asymmetry for breaker bar morphodynamics (Elgar *et al.*, 2001; Hoefel
 894 and Elgar, 2003). The bed slope is another parameter that significantly affects bedload transport rates and
 895 bar morphodynamics in the present experiment.

896 Sand grains in the bed experience two fluid forces acting in cross-shore direction: an inertia or pressure
 897 force by horizontal pressure gradients dp/dx , and a drag force due to the shear stress exerted by the flow
 898 (e.g. Cox *et al.*, 1991). For individual sand grains under surf zone waves, the drag force exceeds the inertia
 899 force by orders of magnitude (Cox *et al.*, 1991). However, pressure forces can penetrate into the bed and
 900 can exert a force over a layer of $O(10D_{50})$ thickness, causing the sand bed to erode as a block rather than as
 901 individual grains (Zala Flores and Sleath, 1998; Sleath, 1999; Foster *et al.*, 2006). The occurrence of such
 902 ‘plug flows’ can be predicted based on the Sleath parameter $S(t) = \rho(du/dt)/(g(\rho_s - \rho))$, where ρ and ρ_s are
 903 the densities of water and sediment, respectively, and the Shields parameter θ (Foster *et al.*, 2006; Cheng
 904 *et al.*, 2016). At the breaking point ($x = 53.0$ m), where the wave is steepest and the highest horizontal
 905 pressure gradients are found, maximum $S = 0.30$ and maximum $\theta = 2.2$ (using Equation 7 for f_w while
 906 excluding acceleration skewness effects, i.e. $T_a/T_{hc} = 0.5$). This is above the threshold proposed by Foster
 907 *et al.* (2006) based on observations under progressive surface waves (i.e. $S > 0.1$) and very close to the
 908 threshold found by Cheng *et al.* (2016) based on detailed numerical simulations (i.e. $0.053\theta + S > 0.426$).
 909 Nevertheless, no evidence for plug flow was found in the present study: the bed erodes layer-by-layer and
 910 not as a block, and sheet flow thicknesses are quantitatively similar to non-breaking wave and oscillatory
 911 tunnel sheet flows. In such sheet flow layers we may expect the fluid drag force to be the main driver for
 912 the horizontal transport of sand grains, although pressure forces may contribute to the initial mobilization
 913 (Calantoni and Puleo, 2006). The sheet flow layer grows due to dispersive inter-particle forces, that lead to
 914 upward transmittal of sand grains as long as the velocity shear layer (i.e. $d|u|/d\zeta > 0$) sustains (Bagnold,
 915 1954; Sleath, 1999).

916 The CCM⁺ measurements show a simultaneous concentration decrease in the sheet flow erosion layer and
 917 a concentration increase in the upper sheet flow layer. The local time-varying sediment load between $\zeta = -$
 918 3 mm and +5 mm, quantified through depth-integration of $\langle C(\zeta, t) \rangle$, remained at both CCM⁺ locations
 919 roughly constant throughout the wave cycle. This confirms that the intra-wave growth and decay of the
 920 sheet flow layer is primarily due to local vertical sediment exchange processes (i.e. sediment pick-up,
 921 vertical advection and diffusion inside the sheet flow layer, and settling), with limited contributions by
 922 horizontal sediment influx from adjacent cross-shore locations. In addition, no evident effects related to the
 923 presence of breaking-generated turbulence or to the bed slope are found. Instead, the sheet flow layer
 924 thickness at the bar crest can be reasonably well predicted based on local phase-averaged velocity using
 925 existing empirical formulations that were originally developed for non-breaking wave and oscillatory flow
 926 tunnel sheet flows. It is reasonable to assume that, within the range of hydrodynamic and bed conditions

927 examined, also existing models for sheet flow transport that are based on local velocity forcing are valid
 928 for the bar crest region in the wave breaking zone.

929 Interestingly, the estimated bedload transport rates along the shoreward bar slope are directed onshore,
 930 while near-bed velocities are directed offshore during almost the entire wave cycle. Hence, bed shear by
 931 phase-averaged velocities cannot be the only mobilizer of bedload particles and instead, bed slope and
 932 possibly breaking-generated TKE have significant effects (**Figure 10**). Physically, the effects of breaking-
 933 generated turbulence on bedload transport are explained as follows. Small-scale wave flume observations
 934 revealed that the intermittent arrival of breaking-generated turbulence at the bed can result in instantaneous
 935 bed shear stresses in both onshore and offshore direction with magnitudes several times the time- and phase-
 936 averaged bed shear stress (Cox and Kobayashi, 2000; Sumer *et al.*, 2013). The occurrence of such
 937 intermittent turbulence events at the bed is random, i.e. it does not correlate with a specific phase of the
 938 wave cycle (Cox and Kobayashi, 2000). The intermittent large bed shear stresses will mobilize particles
 939 which on a sloping bed will be transported downslope by gravity. Such a combined effect by TKE and bed
 940 slope may be the physical mechanism behind the observed onshore transport along the lee-side of the bar
 941 in the present study. Such transport could for instance be modeled as a separate component to bedload
 942 transport using a deterministic formulation with bed slope and breaking-generated turbulence as main input
 943 parameters (e.g. Fernández-Mora *et al.*, 2015). Note that the correlations between bedload transport rates
 944 and forcing parameters (Section 4.4) are relatively low due to the measurement uncertainties in q_{bed} and the
 945 relatively narrow range of variation of the hydrodynamic parameters for one wave condition. Additional
 946 physical or numerical experiments would be required to further understand the effects of breaking-
 947 generated turbulence on bedload transport and to account for these effects in bedload transport models.

948 Although the sand was well-sorted, evident cross-shore grain size sorting was observed and could be related
 949 to size-selective transport both as bedload and as suspended load. This is consistent with combined
 950 experimental-numerical investigations of breaker bar morphodynamics for moderately sorted (Broekema
 951 *et al.*, 2016) and bimodal sands (Srisuwan *et al.*, 2015; Srisuwan and Work, 2015). Our study differs in that
 952 the bed and suspended load transport rates are directly inferred from the measurements and offers additional
 953 insights in local sorting processes around the breaker bar. The samples of suspended sand particles reveal
 954 size-selective pick-up and vertical sorting at the rippled-bed inner surf zone, but approximately size-
 955 indifferent entrainment and mixing in the breaking region, likely due to energetic large-scale vortices.
 956 Although existing models can reproduce the cross-shore grain sorting around laboratory breaker bars
 957 reasonably well (c.f. Srisuwan and Work, 2015; Broekema *et al.*, 2016), the present measurements suggest
 958 that model formulations for size-selective pick-up may be further improved by accounting for the size-
 959 indifferent pick-up under plunging waves.

960

961 **8. Conclusions**

962 We present measurements of sand transport processes and transport rates along an evolving medium-sand
 963 breaker bar under a large-scale plunging breaking wave. Measurements of the sheet flow layer were
 964 obtained at two cross-shore locations near the crest of the breaker bar using CCM⁺. Grain size sorting was
 965 studied through samples of suspended sediment and of the sand bed. The total transport rate was split into
 966 a depth-integrated suspended transport rate and a bedload transport rate, which were both assessed to obtain
 967 a complete overview of the governing transport contributions to breaker bar development. From the results
 968 we conclude:

- 969 1. The sheet flow layer near the bar crest responds quasi-instantaneously to local velocity forcing and
 970 does not reveal significant effects by breaking-generated turbulence. Wave asymmetry (velocity

971 and acceleration skewness) leads to significantly higher sheet flow thickness during the wave crest
 972 phase than during the trough phase, especially at the wave breaking point. The sheet flow layer
 973 thickness can be adequately predicted using existing parameterizations based on local phase-
 974 averaged velocity. The time-varying transport rate depth-integrated over the sheet flow layer is of
 975 similar magnitude as the time-varying suspended sediment transport rate.

- 976 2. The net (i.e. wave-averaged) total transport rate consists of a generally onshore-directed bedload
 977 and an offshore-directed suspended load component, which are of similar magnitude. Bedload
 978 transport dominates at the shoaling zone, decreases at the bar crest, and increases again at the
 979 shoreward facing bar slope. The latter is explained by bed slope effects (i.e. gravity-driven
 980 transport) and occurs in the presence of high near-bed turbulent kinetic energy, which possibly
 981 enhances the mobilization of sand grains. Due to increased suspended sediment load and undertow
 982 magnitudes, suspended transport dominates over bedload transport in the breaking and inner surf
 983 zones. Consequently, near the plunge point the net total transport reverses from onshore-directed
 984 (shoaling zone) to offshore-directed (breaking and inner surf zone).
- 985 3. During the experiment, the breaker bar crest increases in height while the bar trough deepens. Both
 986 bedload and suspended sediment transport contribute to breaker bar morphodynamics, but their
 987 effects are notably different. Bedload transport leads to erosion of the offshore slope and accretion
 988 at the bar crest, and additionally leads to erosion of the steep shoreward bar slope and deposition at
 989 the bar trough. Suspended transport induces erosion of the bar trough, offshore and upward
 990 advection of sediment by the undertow along the shoreward bar slope, and net deposition at the
 991 breaker bar crest.
- 992 4. Suspended sediment samples show evidence of vertical grain sorting at the shoaling and inner surf
 993 zone, which indicates that sediment pick-up and vertical mixing is size-selective (i.e. the fraction
 994 of fine sediment increases with elevation). This contrasts with the breaking region, where sediment
 995 pick-up and vertical mixing is size-indifferent due to the large-scale energetic vortices (strong
 996 upward forcing). Bed samples reveal cross-shore sorting of sand particles by size-selective
 997 transport as bedload and suspended load. This sorting leads to a gradual increase in sediment size
 998 from shoaling to inner surf zone and reveals additional local sorting around the breaker bar due to
 999 bed slope effects (i.e. downward coarsening along the steep shoreward bar slope).

1000 Measurements from the same experiment were used previously to study the effects of wave breaking on
 1001 wave bottom boundary layer hydrodynamics (van der Zanden *et al.*, 2016) and on suspended sediment
 1002 processes (van der Zanden *et al.*, 2017). All combined, the studies offer a detailed insight into the complex
 1003 spatiotemporally-varying hydrodynamics and sediment dynamics along a breaker bar under a plunging
 1004 wave. Upon completion of the project, the data will be disseminated to the scientific community.

1005

1006 **Acknowledgments**

1007 The authors wish to thank the staff of CIEMLAB, in particular Joaquim Sospedra, Oscar Galego and
 1008 Ricardo Torres, for their hospitality and hard work during the experimental campaign. We thank Sjoerd van
 1009 Til for his contributions to the grain size analysis. The authors are also grateful to fellow SINBAD
 1010 researchers for their feedback on preliminary results and to two anonymous reviewers for their constructive
 1011 feedback on the draft manuscript. The research presented in this paper is part of the SINBAD project,
 1012 funded by STW (12058) and EPSRC (EP/J00507X/1, EP/J005541/1). We further acknowledge the
 1013 European Community's FP7 project Hydralab IV (contract no. 261520) for funding the accompanying
 1014 SandT-Pro experiments.

1015

1016

1017 **References**

- 1018 Bagnold, R. A. (1954). Experiments on a Gravity-Free Dispersion of Large Solid Spheres in a Newtonian
 1019 Fluid under Shear. *Proceedings of the Royal Society A: Mathematical, Physical and Engineering*
 1020 *Sciences*, 225(1160), 49-63. doi:10.1098/rspa.1954.0186
- 1021 Baldock, T. E., J. M. Alsina, I. Caceres, D. Vicinanza, P. Contestabile, H. Power and A. Sanchez-Arcilla
 1022 (2011). Large-scale experiments on beach profile evolution and surf and swash zone sediment
 1023 transport induced by long waves, wave groups and random waves. *Coastal Engineering* **58**(2):
 1024 214-227. doi: 10.1016/j.coastaleng.2010.10.006.
- 1025 Battjes, J. A. (1974). Surf Similarity. *Proceedings of the 14th International Conference on Coastal*
 1026 *Engineering*. Copenhagen, Denmark, American Society of Civil Engineers: 466-480
- 1027 Beckman Coulter Inc (2008). Manual LS 13 320 Particle Size Analyzer: 235
- 1028 Blott, S. J. and K. Pye (2001). GRADISTAT: a grain size distribution and statistics package for the
 1029 analysis of unconsolidated sediments. *Earth Surface Processes and Landforms* **26**(11): 1237-
 1030 1248. doi: 10.1002/esp.261.
- 1031 Broekema, Y. B., Giardino, A., van der Werf, J. J., van Rooijen, A. A., Voudoukas, M. I., and B.C. van
 1032 Prooijen (2016). Observations and modelling of nearshore sediment sorting processes along a
 1033 barred beach profile. *Coastal Engineering*, 118, 50-62. doi:10.1016/j.coastaleng.2016.08.009
- 1034 Calantoni, J. and J.A. Puleo (2006). Role of pressure gradients in sheet flow of coarse sediments under
 1035 sawtooth waves. *Journal of Geophysical Research*, 111(C1). doi:10.1029/2005jc002875
- 1036 Cheng, Z., T.-J. Hsu and J. Calantoni (2016). SedFoam: A multi-dimensional Eulerian two-phase model
 1037 for sediment transport and its application to momentary bed failure. *Coastal Engineering*. doi:
 1038 10.1016/j.coastaleng.2016.08.007
- 1039 Cox, D. T., Kobayashi, N. and H. Mase (1991). Effects of fluid accelerations on sediment transport in surf
 1040 zones. *Proc. Coastal Sediments*, Seattle, USA, 447-461.
- 1041 Cox, D. T. and N. Kobayashi (2000). Identification of intense, intermittent coherent motions under
 1042 shoaling and breaking waves. *Journal of Geophysical Research-Oceans* **105**(C6): 14223-14236.
 1043 doi: 10.1029/2000JC900048.
- 1044 da Silva, P. A., A. Temperville and F. Seabra Santos (2006). Sand transport under combined current and
 1045 wave conditions: A semi-unsteady, practical model. *Coastal Engineering* **53**(11): 897-913. doi:
 1046 10.1016/j.coastaleng.2006.06.010.
- 1047 Davies, A. G. and P. D. Thorne (2016). On the suspension of graded sediment by waves above ripples:
 1048 Inferences of convective and diffusive processes. *Continental Shelf Research* **112**: 46-67. doi:
 1049 10.1016/j.csr.2015.10.006.
- 1050 de Meijer, R. J., J. Bosboom, B. Cloin, I. Katopodi, N. Kitou, R. L. Koomans and F. Manso (2002).
 1051 Gradation effects in sediment transport. *Coastal Engineering* **47**(2): 179-210. doi: 10.1016/s0378-
 1052 3839(02)00125-4.
- 1053 Dohmen-Janssen, C. M. and D. M. Hanes (2002). Sheet flow dynamics under monochromatic
 1054 nonbreaking waves. *Journal of Geophysical Research* **107**(C10). doi: 10.1029/2001jc001045.
- 1055 Dohmen-Janssen, C. M. and D. M. Hanes (2005). Sheet flow and suspended sediment due to wave groups
 1056 in a large wave flume. *Continental Shelf Research* **25**(3): 333-347. doi:
 1057 10.1016/j.csr.2004.10.009.
- 1058 Drake, T. G. and J. Calantoni (2001). Discrete particle model for sheet flow sediment transport in the
 1059 nearshore. *Journal of Geophysical Research*, 106(C9), 19859. doi:10.1029/2000jc000611
- 1060 Dubarbier, B., B. Castelle, V. Mariou and G. Ruessink (2015). Process-based modeling of cross-shore
 1061 sandbar behavior. *Coastal Engineering* **95**: 35-50. doi: 10.1016/j.coastaleng.2014.09.004.

- 1062 Dally, W. R. and R. G. Dean (1984). Suspended Sediment Transport and Beach Profile Evolution. *Journal*
 1063 *of Waterway Port Coastal and Ocean Engineering-Asce*, 110(1), 15-33.
 1064 doi:10.1061/(ASCE)0733-950X(1984)110:1(15)
- 1065 Dalrymple, R. A. (1992). Prediction of Storm/Normal Beach Profiles. *Journal of Waterway, Port, Coastal,*
 1066 *and Ocean Engineering*, 118(2), 193-200. doi:10.1061/(asce)0733-950x(1992)118:2(193)
- 1067 Dean, R. G. (1973). Heuristic models of sand transport in the surf zone. Paper presented at the Proc. Conf.
 1068 Eng. Dynamics in the Surf Zone, Sydney, Australia.
- 1069 Dean, R. G., and R. A. Dalrymple (2001). *Coastal Processes with Engineering Applications*. Cambridge
 1070 university press.
- 1071 Dyhr-Nielsen, M. and T. Sorensen (1970). Some sand transport phenomena on coasts with bars.
 1072 Proceedings of the 12th International Conference on Coastal Engineering. Washington, D.C. **54**:
 1073 855-865
- 1074 Elgar, S. (1987). Relationships involving third moments and bispectra of a harmonic process. *IEEE*
 1075 *Transactions on Acoustics, Speech, and Signal Processing*, ASSP-35(12), 1725-1726.
- 1076 Elgar, S., E. L. Gallagher and R. T. Guza (2001). Nearshore sandbar migration. *Journal of Geophysical*
 1077 *Research* **106**(C6): 11623. doi: 10.1029/2000jc000389.
- 1078 Eshel, G., G. J. Levy, U. Mingelgrin and M. J. Singer (2004). Critical Evaluation of the Use of Laser
 1079 Diffraction for Particle-Size Distribution Analysis. *Soil Science Society of America Journal*
 1080 **68**(3): 736. doi: 10.2136/sssaj2004.7360.
- 1081 Fernández-Mora, A., D. Calvete, A. Falqués and H. E. de Swart (2015). Onshore sandbar migration in the
 1082 surf zone: New insights into the wave-induced sediment transport mechanisms. *Geophysical*
 1083 *Research Letters* **42**(8): 2869-2877. doi: 10.1002/2014gl063004.
- 1084 Finn, J. R., M. Li and S. V. Apte (2016). Particle based modelling and simulation of natural sand
 1085 dynamics in the wave bottom boundary layer. *Journal of Fluid Mechanics* **796**: 340-385. doi:
 1086 10.1017/jfm.2016.246.
- 1087 Foster, D. L., R. A. Beach and R. A. Holman (2006). Turbulence observations of the nearshore wave
 1088 bottom boundary layer. *Journal of Geophysical Research-Oceans* 111(C4). doi:
 1089 10.1029/2004jc002838
- 1090
- 1091 Grasmeijer, B. T. and L. C. Van Rijn (1997). Sand transport over a breaker bar in the surf zone. *Coastal*
 1092 *Dynamics*. Plymouth, UK: 88-98
- 1093 Hassan, W. N. and J. S. Ribberink (2005). Transport processes of uniform and mixed sands in oscillatory
 1094 sheet flow. *Coastal Engineering* **52**(9): 745-770. doi: 10.1016/j.coastaleng.2005.06.002.
- 1095 Hassan, W. N. M. (2003). Transport of size-graded and uniform sediment under oscillatory sheet-flow
 1096 conditions. PhD Thesis, University of Twente.
- 1097 Henderson, S. M., J. S. Allen and P. A. Newberger (2004). Nearshore sandbar migration predicted by an
 1098 eddy-diffusive boundary layer model. *Journal of Geophysical Research* **109**(C6). doi:
 1099 10.1029/2003jc002137.
- 1100 Hoefel, F. and S. Elgar (2003). Wave-induced sediment transport and sandbar migration. *Science*
 1101 **299**(5614): 1885-1887. doi: 10.1126/science.1081448.
- 1102 Hsu, T.-J., S. Elgar and R. T. Guza (2006). Wave-induced sediment transport and onshore sandbar
 1103 migration. *Coastal Engineering* **53**(10): 817-824. doi: 10.1016/j.coastaleng.2006.04.003.
- 1104 Hurther, D., Thorne, P. D., Bricault, M., Lemmin, U., and J. M. Barnoud (2011). A multi-frequency
 1105 Acoustic Concentration and Velocity Profiler (ACVP) for boundary layer measurements of fine-
 1106 scale flow and sediment transport processes. *Coastal Engineering*, 58(7), 594-605. doi:DOI
 1107 10.1016/j.coastaleng.2011.01.006
- 1108 Kleinhans, M. G. (2004). Sorting in grain flows at the lee side of dunes. *Earth-Science Reviews* **65**(1-2):
 1109 75-102. doi: 10.1016/s0012-8252(03)00081-3.
- 1110 Koomans, R. L. (2000). Sand in motion: effects of density and grain size, Rijksuniversiteit Groningen, the
 1111 Netherlands.

- 1112 Kraus, N. C., and M. Larson (1988). Beach profile change measured in the tank for large waves 1956-
 1113 1957 and 1962. US Army Corps of Engineers, Coastal Engineering Research Center. Document
 1114 number CERC-88-6.
- 1115 Kriebel, D. L., Dally, W. R. and R. G. Dean (1986). Undistorted Froude model for surf zone sediment
 1116 transport. Proc. 20th Int. Conf. on Coastal Eng, Taipei, Taiwan. 1296-1310
- 1117 Lanckriet, T., J. A. Puleo and N. Waite (2013). A Conductivity Concentration Profiler for Sheet Flow
 1118 Sediment Transport. IEEE Journal of Oceanic Engineering **38**(1): 55-70. doi:
 1119 10.1109/joe.2012.2222791.
- 1120 Lanckriet, T. and J.A. Puleo (2015). A semianalytical model for sheet flow layer thickness with
 1121 application to the swash zone. Journal of Geophysical Research-Oceans, 120(2), 1333-1352. doi:
 1122 10.1002/2014jc010378
- 1123 Lippmann, T. C. and R. A. Holman (1990). The spatial and temporal variability of sand bar morphology.
 1124 Journal of Geophysical Research **95**(C7): 11575. doi: 10.1029/JC095iC07p11575.
- 1125 McLean, S. R., J. S. Ribberink, C. M. Dohmen-Janssen and W. N. Hassan (2001). Sand Transport in
 1126 Oscillatory Sheet Flow with Mean Current. Journal of Waterway, Port, Coastal, and Ocean
 1127 Engineering **127**(3): 141-151. doi: 10.1061/(asce)0733-950x(2001)127:3(141).
- 1128 Murray, S. P. (1967). Control of Grain Dispersion by Particle Size and Wave State. The Journal of
 1129 Geology **27**(5): 612-634. doi.
- 1130 Nielsen, P. (1984). Field-Measurements of Time-Averaged Suspended Sediment Concentrations under
 1131 Waves. Coastal Engineering **8**(1): 51-72. doi: Doi 10.1016/0378-3839(84)90022-X.
- 1132 Nielsen, P. (1992). Coastal Bottom Boundary Layers and Sediment Transport. Singapore, World
 1133 Scientific.
- 1134 O'Donoghue, T. and S. Wright (2004). Concentrations in oscillatory sheet flow for well sorted and graded
 1135 sands. Coastal Engineering **50**(3): 117-138. doi: 10.1016/j.coastaleng.2003.09.004.
- 1136 Peregrine, D. H. (1983). Breaking Waves on Beaches. Annual Review of Fluid Mechanics **15**(1): 149-
 1137 178. doi: 10.1146/annurev.fl.15.010183.001053.
- 1138 Price, T. D. and B. G. Ruessink (2011). State dynamics of a double sandbar system. Continental Shelf
 1139 Research **31**(6): 659-674. doi: 10.1016/j.csr.2010.12.018.
- 1140 Reniers, A. J. H. M., E. L. Gallagher, J. H. MacMahan, J. A. Brown, A. A. van Rooijen, J. S. M. V. de
 1141 Vries and B. C. van Prooijen (2013). Observations and modeling of steep-beach grain-size
 1142 variability. Journal of Geophysical Research-Oceans **118**(2): 577-591. doi: Doi
 1143 10.1029/2012jc008073.
- 1144 Ribberink, J. S. (1998). Bed-load transport for steady flows and unsteady oscillatory flows. Coastal
 1145 Engineering **34**: 59-82. doi.
- 1146 Ribberink, J. S. and A. A. Al-Salem (1994). Sediment transport in oscillatory boundary layers in cases of
 1147 rippled beds and sheet flow. Journal of Geophysical Research **99**(C6): 12707 - 12727. doi:
 1148 10.1029/94jc00380.
- 1149 Ribberink, J. S. and A. A. Al-Salem (1995). Sheet Flow and Suspension of Sand in Oscillatory Boundary-
 1150 Layers. Coastal Engineering **25**(3-4): 205-225. doi: 10.1016/0378-3839(95)00003-T.
- 1151 Ribberink, J. S., J. J. van der Werf, T. O'Donoghue and W. N. M. Hassan (2008). Sand motion induced by
 1152 oscillatory flows: Sheet flow and vortex ripples. Journal of Turbulence **9**(20): 1-32. doi: Doi
 1153 10.1080/14685240802220009.
- 1154 Richmond, B. M. and A. H. Sallenger (1984). Cross-shore transport of bimodal sands. Proc. Coastal
 1155 Engineering Conference: 1997-2008
- 1156 Roelvink, J. A. and A. Reniers (1995). LIP 11D Delta Flume Experiments - Data report. W. D.
 1157 Hydraulics. Delft, The Netherlands: 124
- 1158 Ruessink, B. G., Y. Kuriyama, A. J. H. M. Reniers, J. A. Roelvink and D. J. R. Walstra (2007). Modeling
 1159 cross-shore sandbar behavior on the timescale of weeks. Journal of Geophysical Research
 1160 **112**(F3). doi: 10.1029/2006jfo00730.

- 1161 Ruessink, B. G., H. Michallet, T. Abreu, F. Sancho, D. A. Van der A, J. J. Van der Werf and P. A. Silva
 1162 (2011). Observations of velocities, sand concentrations, and fluxes under velocity-asymmetric
 1163 oscillatory flows. Journal of Geophysical Research **116**(C3). doi: 10.1029/2010jc006443.
- 1164 Sallenger, A. H., R. A. Holman and W. A. Birkemeier (1985). Storm-induced response of a nearshore-bar
 1165 system. Marine Geology **64**: 237-257. doi.
- 1166 Schretlen, J. L. M. (2012). Sand transport under full-scale progressive surface waves. PhD Thesis,
 1167 University of Twente, The Netherlands.
- 1168 Sistermans, P. G. J. (2002). Graded sediment transport by non-breaking waves and currents. PhD thesis,
 1169 TU Delft, the Netherlands.
- 1170 Sleath, J. F. A. (1999). Conditions for plug formation in oscillatory flow. Continental Shelf Research
 1171 **19**(13): 1643-1664. doi: 10.1016/s0278-4343(98)00096-x.
- 1172 Smith, E. R. and N. C. Kraus (1991). Laboratory Study of Wave-Breaking over Bars and Artificial Reefs.
 1173 Journal of Waterway, Port, Coastal, and Ocean Engineering **117**(4): 307-325. doi:
 1174 10.1061/(asce)0733-950x(1991)117:4(307).
- 1175 Srisuwan, C., and P. A. Work (2015). Beach Profile Model with Size-Selective Sediment Transport. II:
 1176 Numerical Modeling. Journal of Waterway, Port, Coastal, and Ocean Engineering, **141**(2),
 1177 04014033. doi:10.1061/(asce)ww.1943-5460.0000274
- 1178 Srisuwan, C., Work, P. A., Karasu, S., and İ. H. Özölçer, (2015). Beach Profile Model with Size-Selective
 1179 Sediment Transport. I: Laboratory Experiment and Sensitivity Study. Journal of Waterway, Port,
 1180 Coastal, and Ocean Engineering, **141**(2), 04014032. doi:10.1061/(asce)ww.1943-5460.0000255
- 1181 Sumer, B. M., L. H. C. Chua, N. S. Cheng and J. Fredsoe (2003). Influence of turbulence on bed load
 1182 sediment transport. Journal of Hydraulic Engineering-Asce **129**(8): 585-596. doi: Doi
 1183 10.1061/(Asce)0733-9429(2003)129:8(585).
- 1184 Sumer, B. M., H. A. A. Guner, N. M. Hansen, D. R. Fuhrman and J. Fredsøe (2013). Laboratory
 1185 observations of flow and sediment transport induced by plunging regular waves. Journal of
 1186 Geophysical Research: Oceans **118**(11): 6161-6182. doi: 10.1002/2013jc009324.
- 1187 Sumer, B. M., A. Kozakiewicz, J. Fredsoe and R. Deigaard (1996). Velocity and Concentration Profiles
 1188 in Sheet-Flow Layer of Movable Bed. Journal of Hydraulic Engineering **122**(10): 549-558. doi:
 1189 10.1061/(asce)0733-9429(1996)122:10(549).
- 1190 Svendsen, I. A., P. A. Madsen and J. Buhr Hansen (1978). Wave characteristics in the surf zone. Proc.
 1191 16th Conf. Coastal Eng. Hamburg, Germany, American Society of Civil Engineers: 520-539
- 1192 Swart, D. H. (1974). Offshore sediment transport and equilibrium beach profiles. PhD Thesis, TU Delft.
- 1193 Thornton, E. B., R. T. Humiston and W. Birkemeier (1996). Bar/trough generation on a natural beach.
 1194 Journal of Geophysical Research-Oceans **101**(C5): 12097-12110. doi: Doi 10.1029/96jc00209.
- 1195 van der A, D. A., T. O'Donoghue and J. S. Ribberink (2009). Sheet flow sand transport processes in
 1196 oscillatory flow with acceleration skewness. Proc. Coastal Sediments 2009, Singapore, World
 1197 Scientific.
- 1198 van der A, D. A., T. O'Donoghue and J. S. Ribberink (2010). Measurements of sheet flow transport in
 1199 acceleration-skewed oscillatory flow and comparison with practical formulations. Coastal
 1200 Engineering **57**(3): 331-342. doi: 10.1016/j.coastaleng.2009.11.006.
- 1201 van der A, D. A., O'Donoghue, T., Davies, A. G., and J. S. Ribberink (2011). Experimental study of the
 1202 turbulent boundary layer in acceleration-skewed oscillatory flow. Journal of Fluid Mechanics,
 1203 **684**, 251-283. doi:10.1017/jfm.2011.300
- 1204 van der A, D. A., J. S. Ribberink, J. J. van der Werf, T. O'Donoghue, R. H. Buijsrogge and W. M.
 1205 Kranenburg (2013). Practical sand transport formula for non-breaking waves and currents.
 1206 Coastal Engineering **76**: 26-42. doi: 10.1016/j.coastaleng.2013.01.007.
- 1207 van der A, D. A., Van der Zanden, J., O'Donoghue, T., Hurther, D., Cáceres, I., McLelland, S. J., &
 1208 Ribberink, J. S. (2017). Large-scale laboratory study of breaking wave hydrodynamics over a
 1209 fixed bar. Journal of Geophysical Research: Oceans, in press. doi:10.1002/2016jc012072

- 1210 van der Werf, J. J., J. J. L. M. Schretlen, J. S. Ribberink and T. O'Donoghue (2009). Database of full-
 1211 scale laboratory experiments on wave-driven sand transport processes. Coastal Engineering
 1212 **56**(7): 726-732. doi: 10.1016/j.coastaleng.2009.01.008.
- 1213 van der Werf, J. J., R. Veen, J. S. Ribberink and J. van der Zanden (2015). Testing of the new SANTOSS
 1214 transport formula in the Delft3D morphological modeling system. Proceedings of Coastal
 1215 Sediments, San Diego, USA: 14 pp.
- 1216 van der Zanden, J., J. M. Alsina, I. Cáceres, R. H. Buijsrogge and J. S. Ribberink (2015a). Bed level
 1217 motions and sheet flow processes in the swash zone: Observations with a new conductivity-based
 1218 concentration measuring technique (CCM+). Coastal Engineering **105**: 47-65. doi:
 1219 10.1016/j.coastaleng.2015.08.009.
- 1220 van der Zanden, J., D. A. Van der A, J. S. Ribberink, T. O'Donoghue, D. Hurther, I. Caceres and P. D.
 1221 Thorne (2015b). Sand transport process measurements under large-scale breaking waves. Proc.
 1222 Coastal Sediments, San Diego, USA: 14 pp.
- 1223 van der Zanden, J., D. A. van der A, D. Hurther, I. Cáceres, T. O'Donoghue and J. S. Ribberink (2016).
 1224 Near-bed hydrodynamics and turbulence below a large-scale plunging breaking wave over a
 1225 mobile barred bed profile. Journal of Geophysical Research: Oceans **121**(8): 6482-6506. doi:
 1226 10.1002/2016jc011909.
- 1227 van der Zanden, J., D. A. Van der A, D. Hurther, I. Caceres, T. O'Donoghue and J. S. Ribberink (2017).
 1228 Suspended sediment transport around a large-scale laboratory breaker bar. Coastal Engineering
 1229 **125**: 51-69. doi: 10.1016/j.coastaleng.2017.03.007
- 1230 Van Rijn, L. C. (1998). The effect of sediment composition on cross-shore bed profiles. Proc. 26th Int.
 1231 Conf. on Coastal Engineering: 2495-2508
- 1232 van Rijn, L. C. (2007). Unified view of sediment transport by currents and waves. III: Graded beds.
 1233 Journal of Hydraulic Engineering-Asce **133**(7): 761-775. doi: 10.1061/(Asce)0733-
 1234 9429(2007)133:7(761).
- 1235 van Rijn, L. C., J. S. Ribberink, J. J. van der Werf and D. J. R. Walstra (2013). Coastal sediment
 1236 dynamics: recent advances and future research needs. Journal of Hydraulic Research **51**(5): 475-
 1237 493. doi: 10.1080/00221686.2013.849297.
- 1238 Wang, P., R. A. Davis and N. C. Kraus (1998). Cross-shore distribution of sediment texture under
 1239 breaking waves along low-wave-energy coasts. Journal of Sedimentary Research **68**(3): 467-506.
 1240 doi.
- 1241 Watanabe, A. and S. Sato (2004). A sheet-flow transport rate for asymmetric, forward-leaning waves and
 1242 currents. Proceedings 29th International Conference on Coastal Engineering, World Scientific. **2**:
 1243 1703-1714
- 1244 Wiberg, P. L., D. E. Drake and D. A. Cacchione (1994). Sediment resuspension and bed armoring during
 1245 high bottom stress events on the northern California inner continental shelf: measurements and
 1246 predictions. Continental Shelf Research **14**(10-11): 1191-1219. doi: 10.1016/0278-
 1247 4343(94)90034-5.
- 1248 Wijnberg, K. M. and A. Kroon (2002). Barred beaches. Geomorphology **48**(1-3): 103-120. doi:
 1249 10.1016/S0169-555x(02)00177-0.
- 1250 Wright, L. D. and A. D. Short (1984). Morphodynamic Variability of Surf Zones and Beaches - a
 1251 Synthesis. Marine Geology **56**(1-4): 93-118. doi: Doi 10.1016/0025-3227(84)90008-2.
- 1252 Zala Flores, N. and J. F. A. Sleath (1998). Mobile layer in oscillatory sheet flow. Journal of Geophysical
 1253 Research: Oceans, 103(C6), 12783-12793. doi:10.1029/98jc00691
- 1254 Zhang, D. P. and T. Sunamura (1994). Multiple bar formation by breaker-induced vortices: a laboratory
 1255 approach. Proc. Intern. Conf. Coastal Eng.: 2856-2870